Title

Time-resolved serial femtosecond crystallography at the European XFEL

Journal

Nature Methods, 17(1)

ISSN

1548-7091

Authors

Pandey, Suraj
Bean, Richard
Sato, Tokushi
et al.

Publication Date

2020

DOI

10.1038/s41592-019-0628-z

Peer reviewed

Published in final edited form as:

Nat Methods. 2020 January ; 17(1): 73–78. doi:10.1038/s41592-019-0628-z.

Time-Resolved Serial Femtosecond Crystallography at the European XFEL

Suraj Pandey[#,1], **Richard Bean**[#,2], **Tokushi Sato**[#,2], **Ishwor Poudyal**[1], **Johan Bielecki**[2], **Jorvani Cruz Villarreal**[3], **Oleksandr Yefanov**[4], **Valerio Mariani**[4], **Thomas A. White**[4], **Christopher Kupitz**[5], **Mark Hunter**[5], **Mohamed H. Abdellatif**[4], **Saša Bajt**[6], **Valerii Bondar**[2], **Austin Echelmeier**[3], **Diandra Doppler**[3], **Moritz Emons**[2], **Matthias Frank**[7], **Raimund Fromme**[3], **Yaroslav Gevorkov**[4,8], **Gabriele Giovanetti**[2], **Man Jiang**[2], **Daihyun Kim**[3], **Yoonhee Kim**[2], **Henry Kirkwood**[2], **Anna Klimovskaia**[2], **Juraj Knoska**[4], **Faisal H. M. Koua**[4], **Romain Letrun**[2], **Stella Lisova**[9], **Luis Maia**[2], **Victoria Mazalova**[4], **Domingo Meza**[10], **Thomas Michelat**[2], **Abbas Ourmazd**[1], **Guido Palmer**[2], **Marco Ramilli**[2], **Robin Schubert**[10], **Peter Schwander**[1], **Alessandro Silenzi**[2], **Jolanta Sztuk Dambietz**[2], **Alexandra Tolstikova**[4], **Henry N. Chapman**[4,12,13], **Alexandra Ros**[3], **Anton Barty**[4], **Petra Fromme**[3], **Adrian P. Mancuso**[2,14], **Marius Schmidt**[*,1]

[1]Physics Department, University of Wisconsin-Milwaukee, 3135 N. Maryland Ave, Milwaukee, Wisconsin 53211, USA

[2]European XFEL GmbH, Holzkoppel 4, D-22869 Schenefeld, Germany

[3]School of Molecular Sciences, and Center for Applied Structural Discovery, The Biodesign Institute, Arizona State University, Tempe, AZ 85287-1604, USA

[4]Center for Free-Electron Laser Science, Deutsches Elektronen Synchrotron, Notkestrasse 85, 22607 Hamburg, Germany

[5]Linac Coherent Light Source, Stanford Linear Accelerator Center (SLAC) National Accelerator Laboratory, 2575 Sand Hill Road, Menlo Park, California 94025, USA

[6]Deutsches Elektronen Synchrotron, Notkestrasse 85, 22607 Hamburg, Germany

[7]Lawrence Livermore National Laboratory, Livermore, CA 94550, USA

[8]Institute of Vision Systems, Hamburg University of Technology, Vision Systems E-2, Harburger Schloßstr. 20, 21079 Hamburg

[9]Physics Department, Arizona State University, Tempe, AZ 85287-1604, USA

[*]Correspondence should be addressed to M.S (smarius@uwm.edu).
[#]These authors have equal contribution.

Author Contributions.

S.P., I.P., M.S. expressed, purified and crystallized the protein. R.B., T.S., J.B., V.B., M.E., G.G., M.J, Y.K., H.K., A.K., R.L., L.M., T.M., G.P., M.R., A.S., J.S.-D., A.M. operated the SPB/SFX instrument. S.L., J.K., R.S., H.C. provided injector nozzles. J.C.V., C.K., M.H., M.A., J.K., F.K., S.L., V.M., D.M., R.S., A.T. collected the data. S.P., I.P., O.Y., V.M., T.A.W., Y.G., A.O., P.S., A.T., A.B. processed the data. S.P., I.P., P.S., A.O., M.S. analyzed the data. C.K., M.A., R.F., P.F. logged the experiment. J.C.V., A.E., D.D., D.K., A.R. conceived and operated the oil co-flow. R.B., T.S., M.F., H.C., A.R., A.B., P.F., A.M., M.S. designed the experiment. S.P., S.B., A.B., P.F., A.M., M.S. wrote the manuscript with input from all other authors.

Competing Financial Interests. The authors declare no competing interests.

[10]Integrated Biology Infrastructure Life-Science Facility at the European XFEL (XBI), Holzkoppel 4, 22869 Schenefeld, Germany

[12]University of Hamburg, Luruper Chaussee 149, 22761 Hamburg, Germany

[13]Centre for Ultrafast Imaging, Luruper Chaussee 149, 22761 Hamburg, Germany

[14]Department of Chemistry and Physics, La Trobe Institute for Molecular Science, La Trobe University, Melbourne, Victoria 3086, Australia

Abstract

The European XFEL (EuXFEL) is a 3.4 km long X-ray source, which produces femtosecond, ultra-brilliant and spatially coherent X-ray pulses at megahertz repetition rates. This X-ray source has been designed to enable the observation of ultrafast processes with near-atomic spatial resolution. Time-resolved crystallographic investigations on biological reactions constitute a particularly important class of experiments with biomedical and health related implications. Due to the unusual X-ray pulse structure, such an experiment is challenging. Here we demonstrate how a biological reaction can be followed on ultrafast time scales at the EuXFEL. We investigate the picosecond time range in the photocycle of photoactive yellow protein (PYP) with MHz X-ray pulse rates. We show that difference electron density maps of excellent quality can be obtained. Results connect the previously explored femtosecond PYP dynamics to time scales accessible at synchrotrons. This opens the door to a wide range of time resolved studies at the EuXFEL.

Time-resolved macromolecular crystallography (TRX) combines macromolecular structure determination with reaction dynamics[1,2]. Short and ultrashort light pulses are employed to enable snapshot observations that cope with the relevant time scales of biomolecular reactions. With TRX, biologically, biomedically and pharmacologically important reactions can be observed in real time with atomic or near- atomic spatial resolution. Hard X-ray free electron lasers (XFELs) substantially changed the way TRX experiments were conducted[3,4] a direct consequence of XFELs' unprecedented brilliance, and their short (femtosecond) X-ray pulses. Instead of examining macroscopically large crystals, microcrystals are injected into the X-ray beam[5,6] at room temperature. Although these microcrystals are often destroyed, the femtosecond X-ray pulse duration at the XFEL largely outruns radiation damage and the associated structural rearrangements[7–10]. Once exposed the XFEL beam, the crystal must be replaced, demanding a serial approach where for each new observation a pristine microcrystal interacts with a subsequent X-ray pulse, a technique known as serial femtosecond crystallography (SFX) [5]. It has been demonstrated recently at the EuXFEL that SFX is possible with megahertz X-ray pulses[11,12], which has been a major milestone. In time-resolved SFX (TR-SFX) a reaction in a microcrystal is initiated with an optical laser during sample delivery into the X-ray interaction volume, and the progress of the reaction is probed after a time-delay Δt by the pulsed XFEL beam as pioneered at the Linac Coherent Light Source (LCLS) at 120Hz[3,4,13,14]. TR-SFX has the potential to take advantage of the megahertz peak rate of the European XFEL to structurally map multiple stages of a reaction with a single experiment.

The experiments reported here examine the photocycle of PYP (Fig. 1a) using the MHz pulse structure of the EuXFEL (Extended Data Fig. 1). PYP is a bacterial photosensor, where the light triggers a reaction with several intermediates[15]. PYP is an excellent model system to establish TR-SFX at the EuXFEL, as it has been previously studied by TRX investigations at both synchrotrons and XFELs[4,14,16,17]. The photocycle is driven by the *trans* to *cis* isomerization of the central para-coumaric acid (pCA) chromophore[18] (Fig. 1b). In addition to being chemically highly important, its ultrafast dynamics displays similarities to other light triggered reactions including the photoisomerization reactions in rhodopsin in the mammalian eye[19] and in other, biologically significant photoreceptors such as the phytochromes[20]. Furthermore, PYP has become a prominent optogenetic tool that can be used for the spatiotemporal optical control of complex biological processes such as neural activity[21]. The photocycle of PYP has been extensively investigated from femtoseconds to seconds[14,17,22]. However, the time-range between 1 ps and 100 ps has so far not been investigated in detail (Fig. 1c) with at least one more process observed by spectroscopy[23] (Fig. 1c, red arrows) for which currently no experimental structural evidence has been provided.

At the EuXFEL X-rays arrive in pulse trains at 10 Hz (Fig. 2a, Extended Data Fig. 1). Each train consisting of bursts of X-ray pulses with an intra-train rate of up to 4.5 MHz[11]. In the current operational configuration, each train contains up to 176 pulses at a maximum rate of 1.13 MHz. This amounts to 1760 pulses per second—already almost 15 times more pulses per unit time than the next highest repetition rate hard X-ray FEL. A high-intensity MHz optical laser system has been commissioned recently and is now available at the SPB/SFX instrument of the EuXFEL[24]. The high pulse repetition rate offers new opportunities for TR-SFX investigations at the EuXFEL. At other XFELs, the low pulse repetition rate limits the amount of data that can be collected during sparsely available beamtimes. With the higher pulse rates at the EuXFEL, closely spaced time-delays can be collected to cover processes in biomolecules in detail. Additional parameters such as temperature[25], laser pulse duration, and laser chirp may then be varied to control [26], and direct the biomolecular reaction.

TR-SFX Experiments.

A dense microcrystalline slurry of PYP was prepared and injected into the vacuum chamber of the SPB/SFX instrument[27] at the EuXFEL. The microcrystals were exposed to the trains of X-ray bursts. X-ray diffraction patterns were collected by the ‘Adaptive Gain Integrating Pixel Detector’ (AGIPD)[28] operating with MHz frame rates (Extended Data Fig. 1). The PYP photocycle was initiated using 240 fs laser pulses at 420 nm wavelength with a flux density of 1.6 mJ/mm^2 in a 42 μm (full width half maximum, FWHM) focal spot. The viscosity of the dense microcrystalline slurry placed an upper limit to the achievable jet speed of 30 m/s (determined in the laboratory under similar injection conditions). Initial measurements were conducted to establish optimal X-ray and laser pulse rates at the achievable jet speed. Laser pulse rates and X-ray pulse structures which were used here are shown in Fig. 2b and c. First, we collected SFX data without any laser excitation at 1.13 MHz X-ray repetition rate to establish a suitable X-ray pulse rate to ensure that the sample was being refreshed between X-ray pulses (Extended Data Table 1, pure ‘dark’). Next, we

exposed crystals to the optical laser at 375 kHz repetition rate (every third X-ray pulse, Fig. 2b, control experiment) to determine when and whether the laser excited jet volume had passed the X-ray interaction region. Data statistics is shown in Extended Data Table 2. With a jet velocity of 30 m/s and laser focus of 42 μm, the excited volume should leave the X-ray interaction region within 2 μs. Accordingly, the difference electron density (DED) map at the 2.67 μs time-delay should be free of signal. However, as shown in Fig. 3, the resulting DED maps display signal at all time-delays. The same density features are observed (see α for negative features, and β1 and β2 for positive features) in all difference maps. All three maps are essentially identical, and contain a mixture of PYP intermediates pR1 and pR2 that persists on the early μs time range[17]. Compare for example the structure displayed in Fig. 3a determined at 1 μs delay at the LCLS[4] with those in Fig. 3b–c. In addition, the hit rate abruptly decayed from 2% at the first X-ray pulse in the train to 1% (Extended Data Fig. 2a) in all subsequent pulses. This shows that jet velocities achievable with our dense PYP slurry do not reliably replace the sample at the X-ray interaction point at the 1.13 MHz X-ray repetition rate. Consequently, both the X-ray pulse repetition rate as well as the laser repetition rate are too high for our planned picosecond TR-SFX experiment. However, there is no indication that there are significant structural differences caused by the 1.13 MHz X-ray pulse rate. R/R-free values of the reference model refined against the data collected in the dark are 17%/24%, respectively, with no obvious differences in F^{obs}-F^{calc} difference maps. It seems that, at least in the case of PYP, the crystals are not affected by acoustic shock-waves observed earlier[29] and the dominant effect is an absence of crystals at the interaction point.

Following these observations, the X-ray repetition rate was reduced to 564 kHz and laser repetition rate reduced to 141 kHz so that laser excitation was achieved before every 4th X-ray pulse, Fig. 2c. At the 0.56 MHz X-ray repetition rate the hit rate across the entire pulse train remains essentially constant (Extended Data Fig. 2b). This shows that at 0.56 MHz the sample is sufficiently refreshed before the next X-ray pulse arrives. The pump-probe delay was set to a value of 10 ps, with subsequent X-ray pulses measuring delays of 1.78 us, 3.56 us and 5.33 us (see Extended Data Table 3 for data statistics). At the 10 ps time delay, we observe a DED map with strong features (Fig. 4a) that resemble the DED map collected at a 3 ps delay at the LCLS (Fig. 5a)[14]. The DED map calculated with data from the following X-ray pulse at 1.78 μs (Fig. 4b) completely differs from the 10 ps DED map,and shows the same pattern of DED features as described in Fig. 3. It can be interpreted with the previously described mixture of intermediates with microsecond lifetimes. The microsecond DED signal decays to a spurious positive feature caused by the displacement of the electron rich Cys-69 sulfur at the 3.56 μs delay (Fig. 4c, blue arrow). This feature vanishes completely at the 5.33 μs delay, which means that a short time after 3.56 μs the laser excited jet volume left the X-ray interaction region. Since the laser profile is Gaussian with a full width at half maximum (FWHM) of 42 μm, there is still substantial intensity in the flanks of the spot that may cause contaminations up to the 3.56 μs time delay. These experiments now demonstrate how the TR-SFX experiment must be set up, when operating within our experimental conditions.

Picosecond Time-Series.

In addition to the 10 ps time point, we collected TR-SFX data sets at 30 ps and 80 ps time delays with the successful timing scheme described. Fluorinated oil was added at various ratios (Extended Data Table 1) via a T-junction to the crystalline slurry (Extended Data Fig. 1). The T-junction was located close to the outside end of the nozzle rod. The oil was co-flown through the long capillary across the rod and injected together with the microcrystals. In addition to a slight increase of the liquid flow rate (Extended Data Table 1), the resulting jets became substantially elongated from previously 100 μm to 700 μm. This allowed us to increase the distance from the nozzle to the interaction region to 400 μm, which helped to prevent the accumulation of debris on the nozzle tip which otherwise would quickly interfere with data collection. The 10 ps to 80 ps time delays cover the region previously unknown in the photocycle probing a time region between the published LCLS data at 3 ps and synchrotron data at 100 ps. Extended Data Table 2 lists the data statistics.

In Fig. 5, the DED maps at 10 ps, 30 ps and 80 ps are shown together with those obtained previously at LCLS and at APS at 3 ps and 100 ps, respectively. In short, all time delays collected at the EuXFEL resulted in excellent DED maps that contain chemically meaningful positive and negative DED features (α and β in Fig. 5). The DED maps (Fig. 5 b–d) are similar and comparable to those obtained at other X-ray sources on the ps time-scale (Fig. 5 a,e). The positive and negative DED features are interpreted by structural models using extrapolated maps[16,30–32] (see Online Methods; Extended Data Tables 4 and 5 list the refinement statistics). In addition to our newly collected time-delays of 10, 30, and 80 ps, we also revisited the 3 ps[14] and the 100 ps[33] data collected previously at LCLS and APS respectively (Extended Data Fig. 3). We subjected all data across the time window from 3 ps to 100 ps to our objective procedures described in the Online Methods to ensure consistent results.

Population transfer (PT) for each time point in this experiment is approximately 7% (see Extended Data Table 6) which is lower compared to similar excitation schemes at other XFELs. With a fs laser pulse we are limited to the primary photo-excitation yield which is 20% at best when excitation is achieved into the absorption maximum[34]. More details on how to estimate the PT are given in the Online Methods. The yield is further diminished here by illuminating into the flanks of the absorption spectrum: excitation was achieved at 420nm rather than into central absorption peak at 450nm (Extended Data Fig. 4b). Still, excellent data can be collected because the laser penetration depth matches the micrometer crystal size[4], leading to uniform sample excitation. From the side view of the pCA chromophore at various time delays in Fig. 5f–j, one can see that the chromophore is in a twisted *cis* configuration throughout. The chromophore head is strongly tilted with the chromophore tail behind the plane of the unexcited (‘dark’) pCA chromophore (see arrows in Fig. 5). Table 1 lists the torsional angle of the chromophore tail φ_{tail} (Fig. 1b) obtained after refinement, as well as the lengths of the H-bonds that fix the chromophore head to Tyr-42 and Glu-46. The revisited φ_{tail} at 3 ps (39°) and 100 ps (30°) agree with results published earlier (35° and 33°, respectively)[14,22].

Discussions

Structural dynamics.

When comparing results at different ps time-delays, the torsional angle at 3 ps (39°) increases at 10 ps (51°), and 30 ps (54°) and relaxes through 80 ps to a final value (30°) at 100 ps. The torsional relaxations up to 3 ps occur in concert with an initial increase of the H-bond distance from the pCA-O_4 to Glu46-O_e (3.3 Å). After 80 ps the H-bonds subsequently relax to shorter distances which approach those observed in the dark structure. Assuming that about half of the absorbed photon energy is stored in the *near-cis* chromophore configuration (on the order of 100 kJ/mol)[35] the release of the chromophore head from a network of two hydrogen bonds should be possible since the energies of the hydrogen bonds are only about 10 kJ/mol[36], each. However, for the pCA head displacements to occur chromophore pocket relaxations are required which are not yet developed on fast time scales. Displacements of the $M_{41–71}$ moiety (Extended Data Fig. 4a) that wraps around the chromophore pocket peak at 10 ps, revert slightly at 30 ps, and slowly increase towards 100 ps (Extended Data Fig. 4c). The initial displacements are reminiscent of ultrafast structural dynamics detected by time-resolved experiments on myoglobin in solution[37]. Although the faster ps time-range (between 1 ps and 100 ps) is sparsely covered by previous experiments[14,22,33] and the experiments at EuXFEL included here, direct structural evidence is provided to show how an energetically highly strained structure initially reorders and then only relaxes slowly for a longer period of time (Extended Data Figs. 4c and 5a,c). It is a direct visualization of a non-exponential, non-ergodic, ultrafast relaxation from a high-energy state towards a longer-lived thermal reservoir, which is structurally characterized by intermediate I_T (Fig. 1a). Only after 100 ps, the PYP molecules that populate this reservoir may sample configurational space more comprehensively to find a reaction coordinate that permits transition to the next intermediate state. As shown previously, transitions to two intermediates (I_{CT} and pR1) are possible[33] requiring reaction coordinates that likely arise from two different positions in configurational space.

Data collection strategy.

In this particular experimental case, reduction of the X-ray pulse repetition rate to 564 kHz was necessary to perform TR-SFX experiments with these dense crystalline slurries with about 30 m/s sample jet speeds. The combination of jet speed and 42 μm (FWHM) laser spots demanded optical laser repetition rates not faster than 141 kHz to minimize contamination from previous exposures. This way, 22 laser pulses are accommodated per X-ray pulse train, which amount to 220 laser excitations per second. This rate is between a factor 3.5 and 15 faster than that achieved previously at other XFELs. To push data collection rates towards the MHz range the liquid flow rate as well as the gas flow rate that narrows the jet to boost its speed [38] must be further increased. If synthetic oil is co-flown with the crystalline slurry, clogging of, and debris deposition on, the GDVN is largely reduced and an increase of the flow rate is possible. With higher gas flow rates, provisions such as increased pump rates to maintain high vacuum levels are required to protect the highly sensitive MHz X-ray detector. When the laser focus is reduced to about 20 μm FWHM, the laser excited jet volume will also leave the X-ray interaction region faster. Then, 564 kHz laser pulses interleaved by 1.13 MHz X-ray pulses will push the speed

of pump-probe data collection rates to the limit and a time-delay can be collected on the order of minutes. Our results also pave the way to collecting X-ray data with femtosecond time-delays at the EuXFEL. At the same time, meaningful datasets on the fast μs time scale may be obtained, which add important time delays and may serve as invaluable controls to assess signal levels in the DED maps. When longer time delays are explored, different strategies with largely reduced laser repetition rates (10 Hz) may be employed where the reaction is initiated already within the nozzle capillary and probed, after injection, by the entire train of X-ray pulses. The MHz data acquisition rate by the pulse trains will be not affected, though, and the time-delays can be swiftly collected.

Future Experiments.

The results of this TR-SFX experiment at the SPB/SFX instrument of the European XFEL demonstrate that with high repetition rate X-ray and optical laser sources which are tunable to the specific rates and energies required for a particular sample or set of measurements, a comprehensive investigation of a macromolecular reaction is possible within a dedicated experimental time including built-in control measurements. This increased data rate may in future allow for the collection of TR-SFX data within very limited experimental time (Extended Data Tab. 6), assuming high uptime of all necessary experimental apparatus. This opens the door to the deployment of enhanced analysis methods to extract macromolecular structures and their dynamics in the crystalline ensemble[39]. This has been achieved on slower time-scales which were covered by dozens[25] of TRX datasets collected over multiple days, and often weeks, of beamtime at synchrotrons[17,25,40]. Close inspection and kinetic interpretation of the TR-SFX data allow an intimate view on mechanical aspects of signal transduction[41] and catalysis[42,43] with specific atomic displacements linked to specific protein function. The close relationship between structural dynamics and function established in this way provide new avenues for the control [26,44,45] and the understanding of biological function, that then also pave the way to a deeper understanding of the mechanism of the bio-macromolecular reaction in bio-medically and biologically highly significant macromolecules.

ONLINE METHODS

Sample Preparation.

PYP was overexpressed and purified as reported[46,47]. PYP microcrystals were grown with the stir-method using 3.3 mol/L malonate (pH 7) as precipitant[46]. PYP was concentrated to 100 mg/mL, and 4 mol/L Na-malonate, pH 7, was added at once to a final concentration of 3.3 mol/L under vigorous stirring. The suspension (20 mL) was stirred in a closed glass vial for 8 h and let rest for an additional 24 h at room temperature. This method works equally well with smaller ~ 2 mL and larger ~ 20 mL volumes. Stirring is necessary to prevent the growth of crystals to sizes larger than 10 μm. The slurry was spun at 8000 g for 10 min. The microcrystals swim up. The clear solution below the microcrystals was removed and replenished by 2.8 mol/L Na-malonate, pH 7. This resulted in a suspension containing about 10^9 to 10^{10} crystals/ml with most crystals being about 5 μm as observed under a microscope with 400 x magnification using a Neubauer cell counting chamber. The dense PYP microcrystalline slurry was filtered twice by handpressing the slurry (placed in a 10

mL syringe) through a 10 μm stainless steel filter. The slurry was injected without further filtering into the vacuum chamber at the SPB/SFX imaging and serial crystallography instrument[48,49] using a gas dynamic virtual nozzle (GDVN)[50] with 75 μm inner diameter (ID) (Extended Data Fig. 1). Smaller nozzle diameters led to clogging and reduced flow rate due to pressure limitations.

Injection and Alignment.

With the 75 μm ID nozzles, we attempted to maximize slurry flow and gas pressure to produce a fast jet that may be able to cope with the enormous X-ray pulse rates. We measured the jet diameter to be about 5 μm with a flow rate of 35 μL/min under identical conditions as used for the experiment (Extended Data Table. 1). This translates into a jet speed of approximately 30 m/s. In order to avoid clogging, for some time-delays, we added an immiscible fluorinated oil mixture (perfluorodecalin and 1H, 1H, 2H, 2H-perfluoro-1-octanol in a 10:1 ratio) through a T-junction (Extended Data Fig. 1) located upstream of the injector nozzle rod at various flow rate ratios (Extended Data Table 1). The GDVN tip surface as well as the capillaries to the GDVN were treated with Novec 1720[51] to stabilize the simultaneous injection with oil and avoid growth of stalactite-like debris on the nozzle which originates from the jet explosion after X-ray exposure. With this treatment, the oil can form a lubricant layer between the walls and the aqueous jet which minimizes interaction and sticking of crystals effectively avoiding clogging. As observed earlier[52], exposure to the intense X-ray pulses resulted in gaps in the jet caused by Coulomb explosion. The PYP photocycle was initiated in microcrystals with 240 fs laser pulses of wavelength 420 nm, which is 30 nm on the blue side of the PYP absorption maximum (Extended Data Fig. 4b). As established earlier by ultrafast spectroscopy on PYP crystals[53], laser excitation (into the absorption maximum) with 1 mJ/mm^2, is essentially free of non-linear effects. This disperses concerns voiced recently on other systems (see Nass Kovacs et al., arXiv:1905.09002). Since the absorption at 420 nm is only 60% of that of the absorption maximum (Extended Data Fig. 4b), we used accordingly 1.6 mJ/mm^2 laser fluence in a 42 μm (FWHM) laser spot. Imaging the gaps in the jet[52] provides a convenient method to align the laser with the X-rays by centering the laser focal spot in the gap. Temperature was not controlled. Laser warming (about 10° C)[54] and evaporative cooling effects (a few degrees) fortuitously compensate. Details of the experimental setup which includes laser setup, laser alignment, the timing and the determination of the temporal overlap of X-ray and laser pulses are listed below.

Instrumentation.

Experiments were performed at the SPB/SFX instrument in March 2019 as a part of proposal 2166 using a similar configuration as used in Wiedorn et.al[52] (Extended Data Fig. 1). The size of the mirror-focused focal spot[55] in the interaction region was estimated to be 2×3 μm FWHM diameter based on optical imaging of single shots using a 20 μm thick Ce:YAG screen. The X-ray pulse energy was about 700 μJ. Diffraction from the sample was measured using an AGIPD [56,57] 1Mpx located 117.7 – 118.6 mm downstream of the sample interaction region, with the unused direct beam passing through a central hole in the detector to a beam stop further downstream (Extended Data Fig. 1). The resolution at the edge of the AGIPD was 1.8 Å, and 1.6 Å data were obtained by integrating Bragg reflections into the

detector corner. Experiment control is provided by Karabo[58] and data acquisition is provided by dedicated technology to cope with the megahertz repetition rates[59].

Laser Setup and Timing.

Optical laser radiation with wavelength 840 nm and 15 fs pulse duration was used to generate a 420 nm second harmonic using a 0.5 mm thick beta barium borate (BBO) crystal. Additionally, fused silica windows and lenses stretched the pulse to 250 fs duration. The beam size at the sample position was measured by a scintillator and simple in-situ microscope yielding a diameter of 42 μm FWHM. The average laser energy was about 2.3 μJ, which corresponds to 1.6 mJ/mm^2 fluence at the sample. The optical laser timing was synchronized with an radio frequency (RF) signal, and timing at the experiment was controlled by a phase shifter. The T0 position, when both optical and X-ray beams arrive simultaneously, was estimated by the spatial encoding method using a $SrTiO_3$ crystal[60]. Both the inter-train timing and the *intra*-train timing were measured earlier in facility experiments. The train arrival time jitter was determined to be ~300fs for the system in RF lock[60]. The intra-train jitter was measured to be significantly shorter than 1 ps, which is then negligible in terms of the ps timing scheme employed here. In addition, we never observed more than 1 ps drift in our RF synchronization over a 12 h shift.

Data processing.

Experiment progress was monitored online using OnDA[61] for serial crystallography. Diffraction images with Bragg reflections were found by Cheetah[62] (peakfinder8, minSNR=8, minADC=200, minPix=1, minPeaks=25) using the calibration process described by Wiedorn et al. [52]. Careful masking of shadowed and unreliable regions of the detector was performed on a run-by-run basis. Independent masks were used for peakfinding to avoid false peaks, for example due to ice formation. Indexing was performed using CrystFEL version 0.8.0 with peaks found by Cheetah using the indexing package XGANDALF. Detector geometry, especially the detector distance was refined using program Geoptimiser[63]. Merging and scaling of the Bragg peaks intensities were performed using the partialator program from CrystFEL. To avoid the integration of noise for weakly scattering patterns, reflections were included up to 1.0 nm^{-1} above a conservative resolution estimate for each crystal (--push-res=1.0). Since PYP crystallizes in $P6_3$, an indexing ambiguity[64] is present[46]. It was corrected by the ambigator module in CrystFEL. Figures of merit were calculated using compare_hkl (Rsplit, $CC_{1/2}$, CC*) and check_hkl (signal-to-noise ratio, multiplicity, completeness), both a part of CrystFEL. The intensities from all indexed patterns were scaled together irrespective of the delay setting. Individual time delays were separated, and their intensity merged. This separation has been achieved based on pulse IDs in the train (see below and Extended Data Fig. 1) which are stored together with the diffraction patterns. The corresponding intensities were then merged to generated reference datasets, and datasets at different time delays, each (Extended Data Tables 1–3).

Pump-Probe Timing Schemes.

X-ray pulses arrive in pulse trains with currently up to 176 X-ray pulses with 1.13 MHz repetition rate within the train. Each train repeats with 10 Hz (Fig. 2a and Extended Data Fig. 1). The tunable, high energy femtosecond laser system installed at the SPB/SFX

instrument[65] is able to cope with the MHz pulse repetition rate. For the various experiments, two different pump-probe timing strategies were used. They are shown in Fig. 2. The laser is synchronized to X-ray pulse #1 in each train whose radio frequency signal is delivered by the EuXFEL control room to the instrument. The X-ray fluence in pulse #1 has been very low for this experiment, and spurious diffraction patterns produced by it are not used. In scheme (1), the X-ray pulse rate is 1.1 MHz (Fig. 2b). The laser is activated 2.3 ns after pulse #1. Accordingly, pulses #2, #3 and #4 probe the reaction after 0.89 μs (887 ns), 1.78 μs and 2.67 μs. This sequence repeats with laser activation after pulse #4, #7, #10 and so on, interleaved with the three μs time delays, each. This results in a Laser pulse repetition rate of 376 kHz, and 176/3 = 58 laser activations per pulse train. The effective laser excitation rate is therefore 580 Hz. As demonstrated in Extended Data Fig. 2a and Fig. 3, both the X-ray repetition rate as well as the intra-train laser repetition rate, respectively, are too large for the jet speeds achieved with the viscous PYP microcrystalline slurry. In scheme (2) the X-ray pulse repetition rate in the train is reduced to 564 kHz with 88 pulses/train (Fig. 2c). This time, the hit rate varies smoothly with the X-ray pulse energy across all X-ray pulses in the train (Extended Data Fig. 2b), no abrupt decay as observed for higher X-ray pulse rates (as in Extended Data Fig. 2a) is observed. The laser is synchronized again with respect to X-ray pulse #1. This time, the synchronization is precisely adjusted, so that the pump-probe delay Δt between the laser pulse and X-ray pulse #2 is on the picosecond time-scale (Fig. 2c) which is necessary to collect data for the 10 ps, 30 ps and 80 ps time delays. As shown for other XFELs, the XFEL to laser timing fluctuations are on the order of 300 fs[66], which is negligible on the ps time-scale, and a timing-tool[67,68] is not required. The next laser pulse arrives after X-ray pulse #5. The laser pulse repetition rate is therefore 141 kHz. Accordingly pulses #2, #6, #10 etc. in the train probe a picosecond time delay, and three additional interleaving X-ray pulses probe time delays at 1.78 μs, 3.56 μs and 5.33 μs. This results in 22 pump-probe sequences with ps time delay per train, and 220 effective laser excitations per second. At the Spring-8 Angstrom Compact Laser (SACLA) and the Linac Coherent Light Source (LCLS), typical X-ray pulse rates are 30 Hz and 120 Hz, respectively. Pump-probe sequences with interleaving dark data collection require 15 Hz or 60 Hz laser pulse rates. Compared to these machines, even with the small number of 88 X-ray pulses in the train in these early experiments, the effective laser repetition rate of scheme (2) is between a factor of 3.5 to 15 faster. In the future, more than one order of magnitude more X-ray pulses will be available per train, which speeds up data collection accordingly. It must be decided on a case by case basis whether MHz pulse rates can be used when low viscosity slurries with small crystals are available that allow narrow GDVN orifices and enable fast jet speeds, or repetition rates of both X-ray and laser pulses must be reduced as in the case of PYP. On the order of 675 X-ray pulses per train with a 1.13 MHz intra-train repetition rate are planned to become available soon. A pump-probe data collection strategy shown in Fig. 2a that contains only one interleaved dark will be feasible. In this case 337 laser pulses per train result in the enormous effective laser excitation rate of 3370 Hz. As the AGIPD measures up to 352 pulses per train, 3520 patterns (out of the 6750) can be stored per second. With a low 2% hit rate and a 50% indexing rate as demonstrated in this paper, the approximately 25000 indexed diffraction patterns which are required to detect low levels of population transfer can be collected in about 20 min. This includes the collection of the reference (dark) data. Protein consumption is about 10% of that expected at

slower XFELs (Extended Data Tab. 6), and should be between 20 mg and 40 mg per time delay depending on the design of the experiment.

Difference map calculation.

A reference (dark state) model M_{ref} is refined by using the program 'refmac'[69] against structure factor (SF) amplitudes collected in the dark $|F_{dark}|$ without laser excitation. To check for spurious features at μs delays, the pure dark data (Extended Data Table 2) were used as a reference. The dark3 data from the 30 ps time-series display superior statistics (Extended Data Table 3), and served as reference for all ps time delays. Model structure factors are calculated from M_{ref} with amplitude $|FC_{ref}|$ and phase ϕ_{ref}. The measured $|F_{dark}|$ are brought to the absolute scale by scaling them to $|FC_{ref}|$ using the CCP4 program 'scaleit'[70]. The time-dependent SF amplitudes $|F_{obs}(t)|$are then scaled to the $|F_{dark}|$in a second run of 'scaleit'. As result, both $|F_{obs}(t)|$ and $|F_{dark}|$ are on the absolute scale, and scaled together. Difference structure factor (DSF) amplitudes are calculated: $DSF_{obs} = |F_{obs}(t)| - |F_{dark}|$. A weighting factor w for the DSFs is determined to reduce the influence of outliers[71]. The DSFs are combined with phases ϕ_{ref}. From the weighted DSFs, a weighted difference electron density (DED) map is calculated using the program 'fft' from the ccp4 suite of programs[70]. Although the |F(obs,t)| and the |Fdark| are on the absolute scale, the difference map is, due to the difference Fourier approximation[72], only on half the absolute scale. The preserved absolute scale is necessary to estimate population transfer levels as explained below. The DED maps are best contoured on the 3 σ/-3 σ levels (Extended Data Fig. 6)

Refinement.

Meaningful negative features in the DED map are necessarily located on top of the reference model M_{ref}. However, contiguous, chemically sensible positive features in the DED map must be interpreted with a new structural model (M_{TRX}). To determine structures from DED maps, extrapolated, conventional electron density (ED_{ext}) maps[73,74] are used. For extrapolated structure factor (SF_{ext}) amplitudes a multiple of the DSFs are added to the $|FC_{ref}|$: $SF_{ext} = |FC_{ref}| + N{*}DSF$ and combined with the reference state (dark) phases ϕ_{ref}. Here the use of $|FC_{ref}|$ derived from an accurately refined dark state model are preferred over the $|F_{dark}|$ as explained by Terwilliger & Berendsen[75]. From the phased SF_{ext}, extrapolated electron density maps (ED_{ext}) are calculated with the ccp4 program 'fft'. A characteristic N_{ext} is established when the electron density in the ED_{ext} at the positions with strong negative features in the DED maps just vanishes. When N is too large, false - negative features will appear in the ED_{ext}. This can be visualized by summing up negative values in the ED_{ext} within a volume that contains strong DED features in the DED maps. Extended Data Fig. 7 shows results for such a summation for all our TR-SFX time-delays collected at the EuXFEL and TRX data selected from the literature[46,74,76]. N_{ext} is marked with an arrow. N_{ext} is approximately related to the population transfer (PT): $PT \sim \frac{100}{N_{ext}} * 2$ [%]. The factor of two accounts for the difference Fourier approximation mentioned above. If the PT is small, N_{ext} is large. N_{ext} = 30 is not uncommon in TRX, especially with fs excitation, since the primary yield of photoactivation can be quite small [77] and is further diminished by experimental circumstances. Once N_{ext} has been established, structural models are

determined from the resulting ED_{ext} maps. The ED_{ext} map is displayed in a molecular modeling program such as 'coot'[78]. The reference model can be used as an initial model for a refinement. When structural changes are small, the initial model is altered by directly refining it against the ED_{ext} map by a stepped real-space refinement in 'coot' with the torsional restraint switched off (default in 'coot'). For PYP, isomerization and structural changes are modelled automatically this way, entirely without manual intervention. For other systems[79] structural changes can be modelled manually in analogy to conventional structure determination. A new structural model M_{TRX} is obtained this way. From the real-space refined M_{TRX} and M_{ref} models, calculated DSF_{calc} can be determined, this time with amplitude and phases ϕ_{Δ}. When the DED_{calc} calculated from the phased difference structure factors is compared to the DED_{obs}, prominent DED features should match (Extended Data Fig. 8). The ϕ_{Δ} are combined with the measured DSF_{obs} and phased extrapolated SFs (pSF) are obtained by adding the (now phased) DSF_{obs} to the FC_{ref} as vectors in the complex plane[80,81]. M_{TRX} is refined against the |pSF| using restrained reciprocal space refinement, using e.g. 'refmac'[69]. Typically, R-factors are acceptable and do not deviate much from those of refinements against conventional X-ray data. Structural models and ED maps are shown in Extended Data Fig. 3. Refinement statistics is shown in Extended Data Tables 4 and 5. Selected model parameters are listed in Table 1 (main text) for the 3 ps to 100 ps time-range.

Displacements and Difference Distance Matrices.

Structural differences were analyzed by calculating the root mean square displacements (RMSDs) of like C_{α} atoms in the $M_{41–71}$ moiety (Extended Data Fig. 4a) between the structures determined at the various time-delays and the reference structure. The RMSD values in Extended Data Fig. 4c were fit by an empirical function consisting of an exponential term, a linear term, and a strongly damped cosine function which includes a phase shift:

$$RMSD_{fit} = A_0\left(1 - e^{\frac{1}{\tau}t}\right) + b \cdot t + A_1\cos\left(\frac{2\pi}{T}t + \varphi\right)e^{-\beta t}$$

The fit values were A_0=0.181 Å, τ=1.4 ps, b=4.5×10^{-3} Å/ps, A_1=0.038 Å, T=50 ps, φ=257°, β=1/50 ps^{-1}. Some of the fit values are not unique. For example, T in the cosine function can vary largely because only a few time delays are available across the 100 ps time scale. T was selected so that the decrease of the RMSD at 30 ps is modeled correctly, and the damping constant β was selected so that the oscillation vanishes quickly. To show more global displacements, difference distance matrices (Extended Data Fig. 5a–d) were calculated[82] using Fortran code of the DDMP program from the Center for Structural Biology at Yale University, New Haven, CT. The calculations include residues 42 to 92 and use the 3 ps structure as a reference (note: if the dark structure would be used as a reference, small structural changes in the time window from 3 ps to 100 ps would not be observable). With these matrices one can also visually identify the decline of the magnitude of the difference distances between 10 ps and 30 ps, and their increase at 100 ps, in particular in

the $M_{41–71}$ region (green bar), and then at 100 ps also more globally in the $H_{74–88}$ region (depicted also in Extended Data Fig. 4a).

Data Availability.

Data has been deposited with the Coherent X-ray Imaging data bank[83] with CXIDB ID 100. This includes: Stream files for all data and for data separated into each time-delay, MTZ and PDB files for all time-delays including the dark/reference structures. We have deposited data (mtz-files and structures) for the 10 ps, 30 ps and 80 ps time-delays, as well as the dark3 (30 ps) and pure dark reference structures to the protein data bank, with deposition codes 6P4I, 6P5D, 6PSE, 6PSG and 6PSF, respectively.

Code Availability.

Linux scripts and Fortran source codes for the calculation of weighted difference maps, extrapolated electron density maps and the integration of negative densities within a spherical volume are included in a demo which is available online as supplementary material.

Extended Data

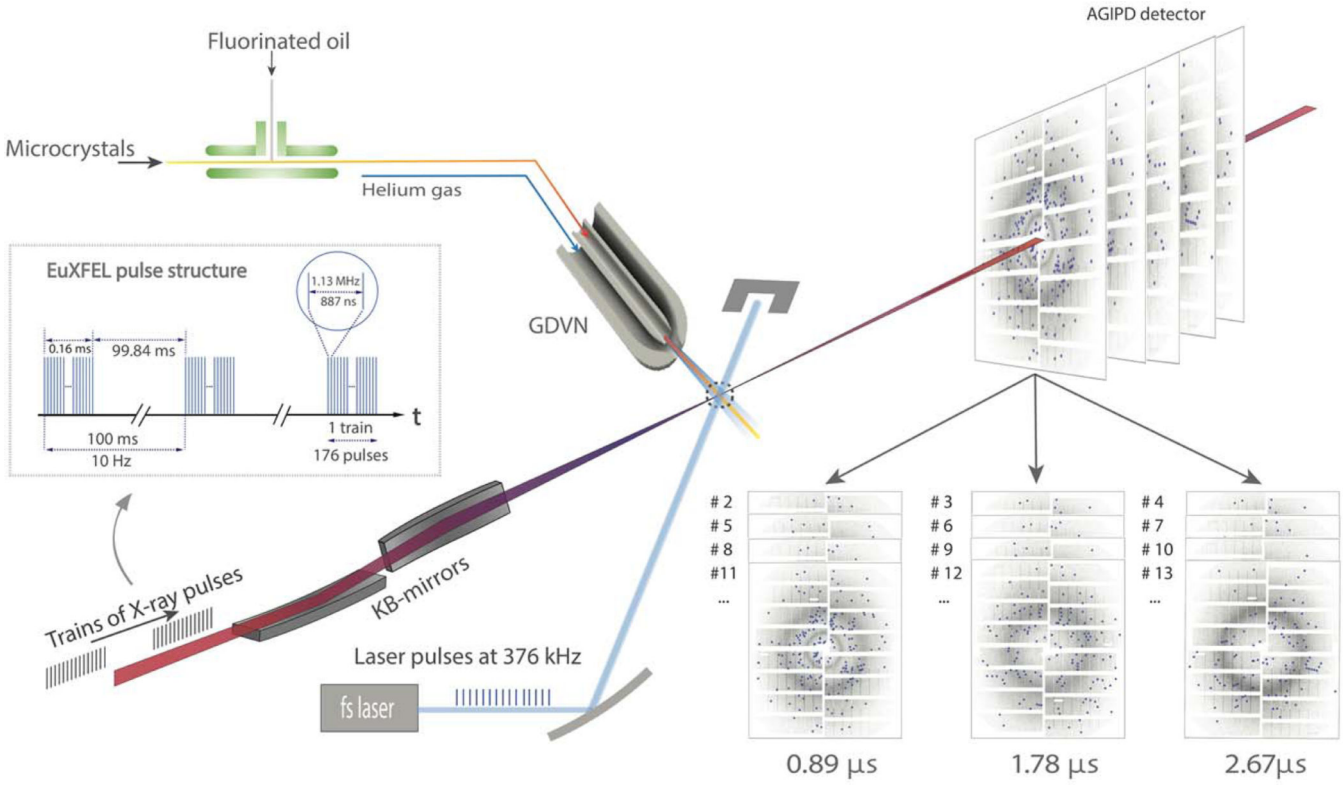

Extended Figure 1. Setup of a MHz TR-SFX experiment at the EuXFEL (modified from Wiedorn et al., 2018)

X-ray pulses arrive in 1.13 MHz bursts which repeat every 100 ms. There are 176 X-ray pulses in the burst. The KB-mirror system focuses the X-ray beam to a 2 – 3 μm focal spot. The fs-laser delivers 376 kHz pulses (λ=420 nm, blue) synchronized to the X-ray pulses.

The laser focus is 42 μm Ø in the X-ray interaction region (dotted circle). The microcrystals are mixed with fluorinated oil and injected by a GDVN. The jet produced by the GDVN, the laser beam as well as the X-ray pulses precisely intersect. The time-resolved diffraction patterns are collected by the AGIPD. Diffraction patterns with common time-delays were separated based on the pulse ID (see also Fig. 2b) and combined to datasets.

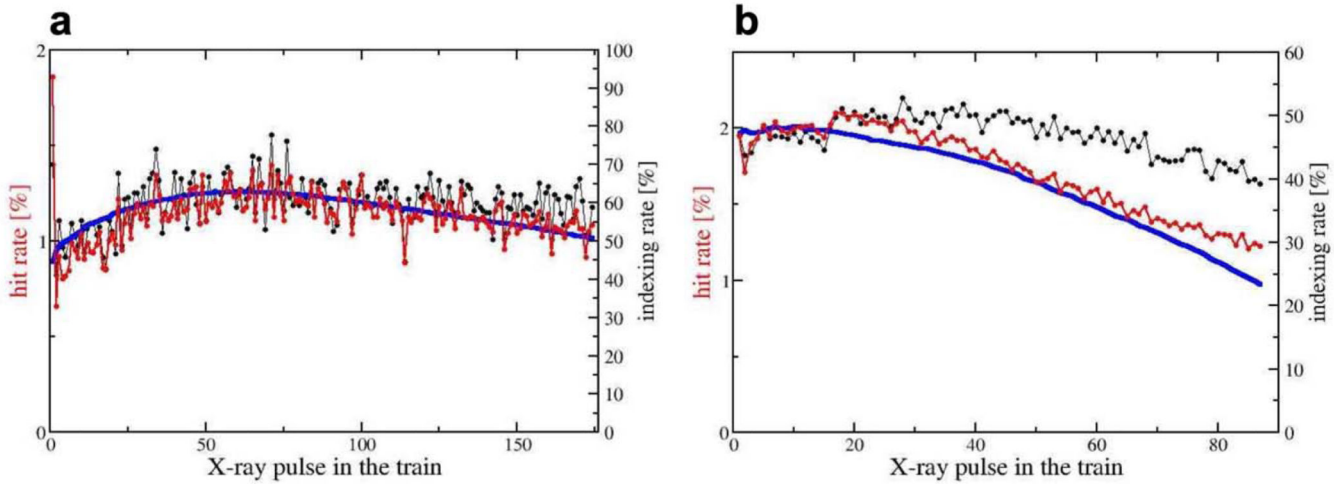

Extended Figure 2. Hit and indexing rates

a, Hit rates (red) and indexing rates (black) with 1.13 MHz X-ray pulse repetition rate. Note, the strong drop of the hit-rate after the first pulse from 2% to 1%. 472,528 total patterns, 41,559 hits and 24,815 indexed patterns were separated on the basis of pulse IDs. From these, hit rates and indexing rates were calculated. **b**, Hit rates (red) and indexing rates (black) with 564 kHz X-ray pulse repetition. The overall hit rate is about 2%. 52,495,158 total patterns, 304,673 hits and 142,948 indexed patterns were separated on the basis of pulse IDs from which hit rates and indexing rates were calculated. Blue solid line in **a** and **b**, X-ray pulse energy (on arbitrary scale). The indexing rate varies only slightly and is about 40% - 60%.

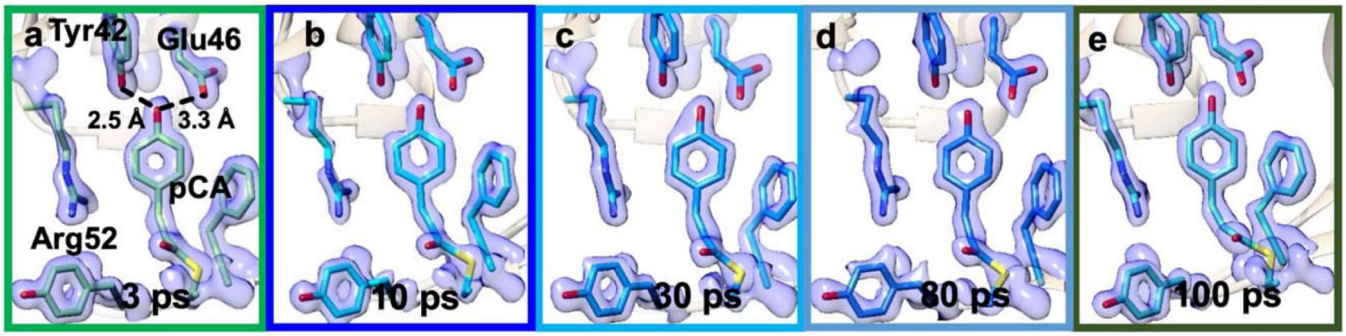

Extended Figure 3. Extrapolated electron density maps (1.5 σ contour level)

a, 3 ps at LCLS (Pande et al., 2016). **b** - **c**, 10 ps, 30 ps and 80 ps at EuXFEL. **e**, 100 ps at APS (Jung et al., 2013). The extrapolated maps were calculated from 13,722, 13,142, 13,014, 12,889 and 13,214 extrapolated structure factors for the 3 ps to 100 ps time delays, respectively.

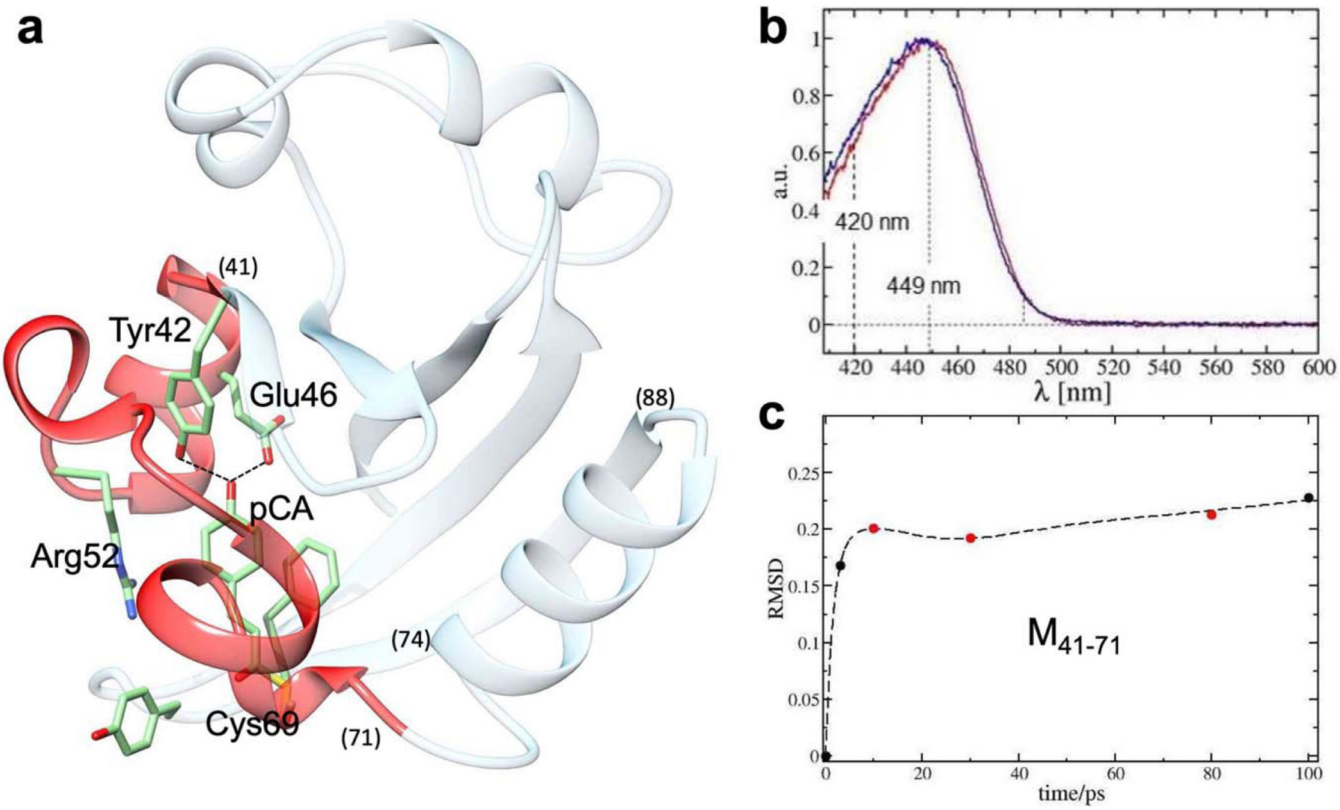

Extended Figure 4. Excitation and ultrafast displacements in PYP.

a, Structure of PYP. Some important residues in the chromophore (pCA) binding pocket are marked. The $M_{41–71}$ moiety (residues 41 to 71) is marked in red. Helix H74–88 is marked. **b**, Dark state spectra of PYP. Black: measured in solution, red: in the crystal. The wavelength at the absorption maximum is marked. Excitation has been achieved with 240 fs laser pulses with λ=420 nm. **c**, Solid spheres: root mean square displacements of 31 Cα atoms in M41–71 relative to the dark (reference) structure, red spheres: from data measured at EuXFEL. Dashed line: fit by a function consisting of an exponential, a strongly damped, phase shifted cosine function and a straight line as outlined in the text.

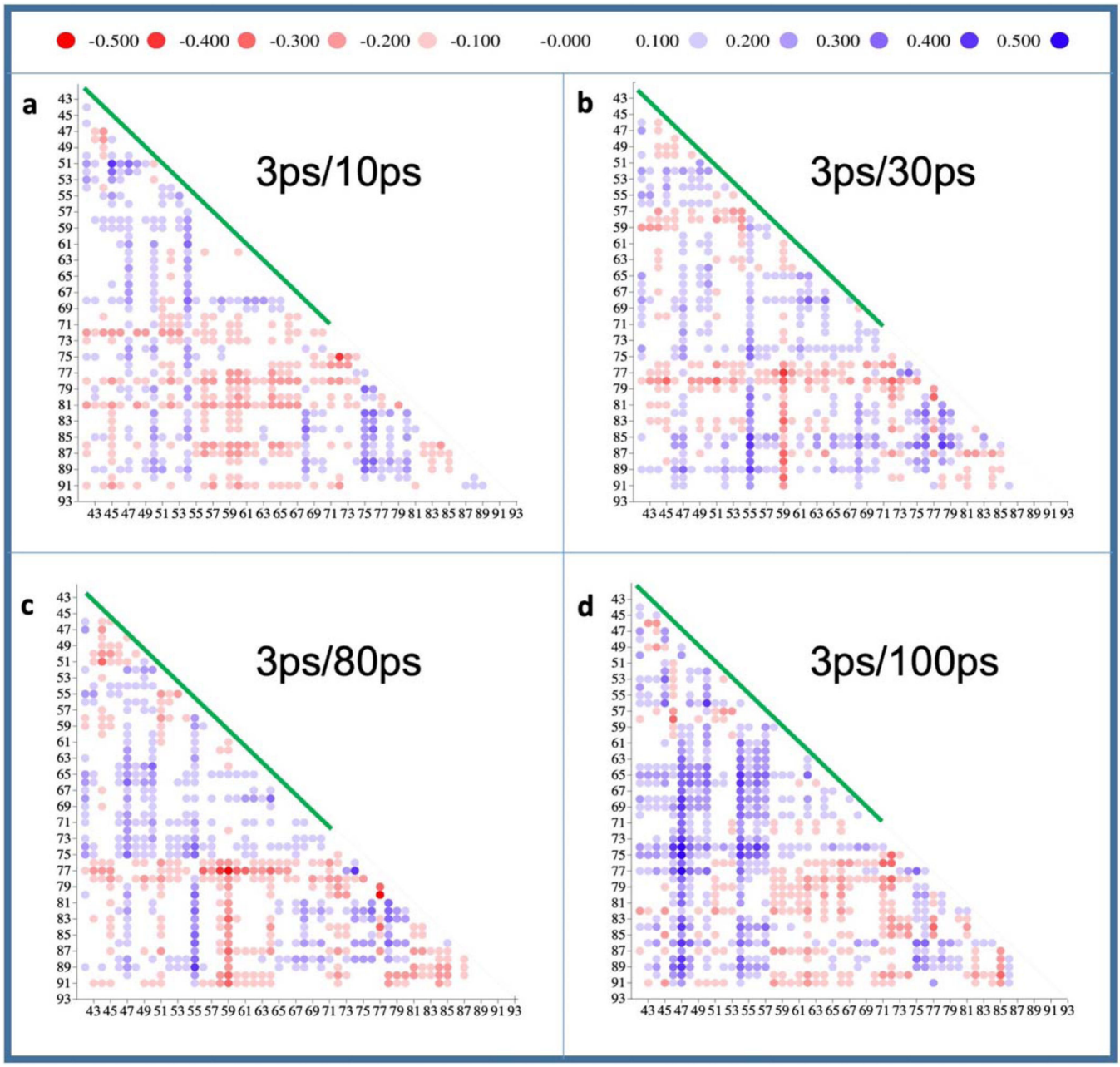

Extended Figure 5. Difference distance matrices evaluated for Cα atoms of residues 42 to 93.

The green line denotes the $M_{41–71}$ moiety. The scale on top is in Å. **a** - **d**, Difference distance matrices derived from structures at 10 ps, 30 ps, 80 ps and 100 ps relative to that at 3 ps, respectively. Difference distances are also shown for helix $H_{74–88}$.

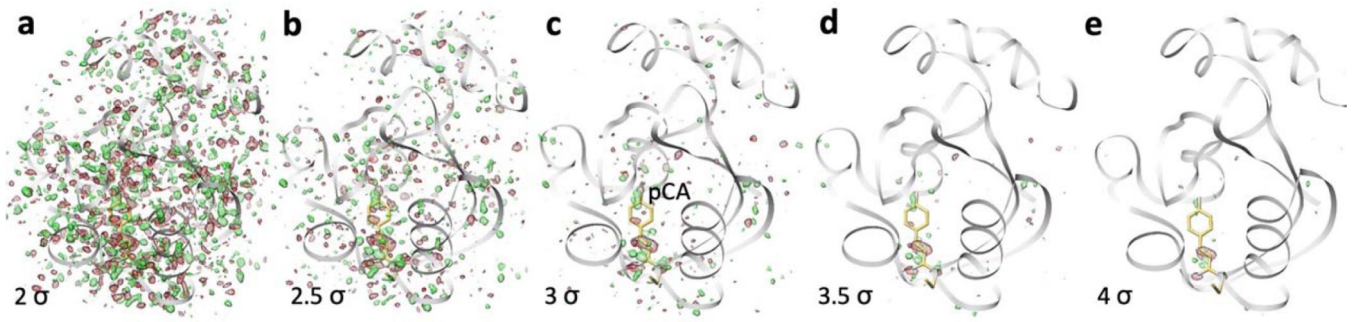

Extended Figure 6. Signal levels in the DED map at the 30 ps delay

The DED map at 30 ps is overlaid on the entire PYP and contoured from +/− 2σ to +/− 4σ in steps of 0.5σ. Red: negative DED, green: positive DED. The 3σ level, c, is the best compromise to distinguish the signal, for example on the pCA chromophore, from spurious noise features distributed within the protein volume.

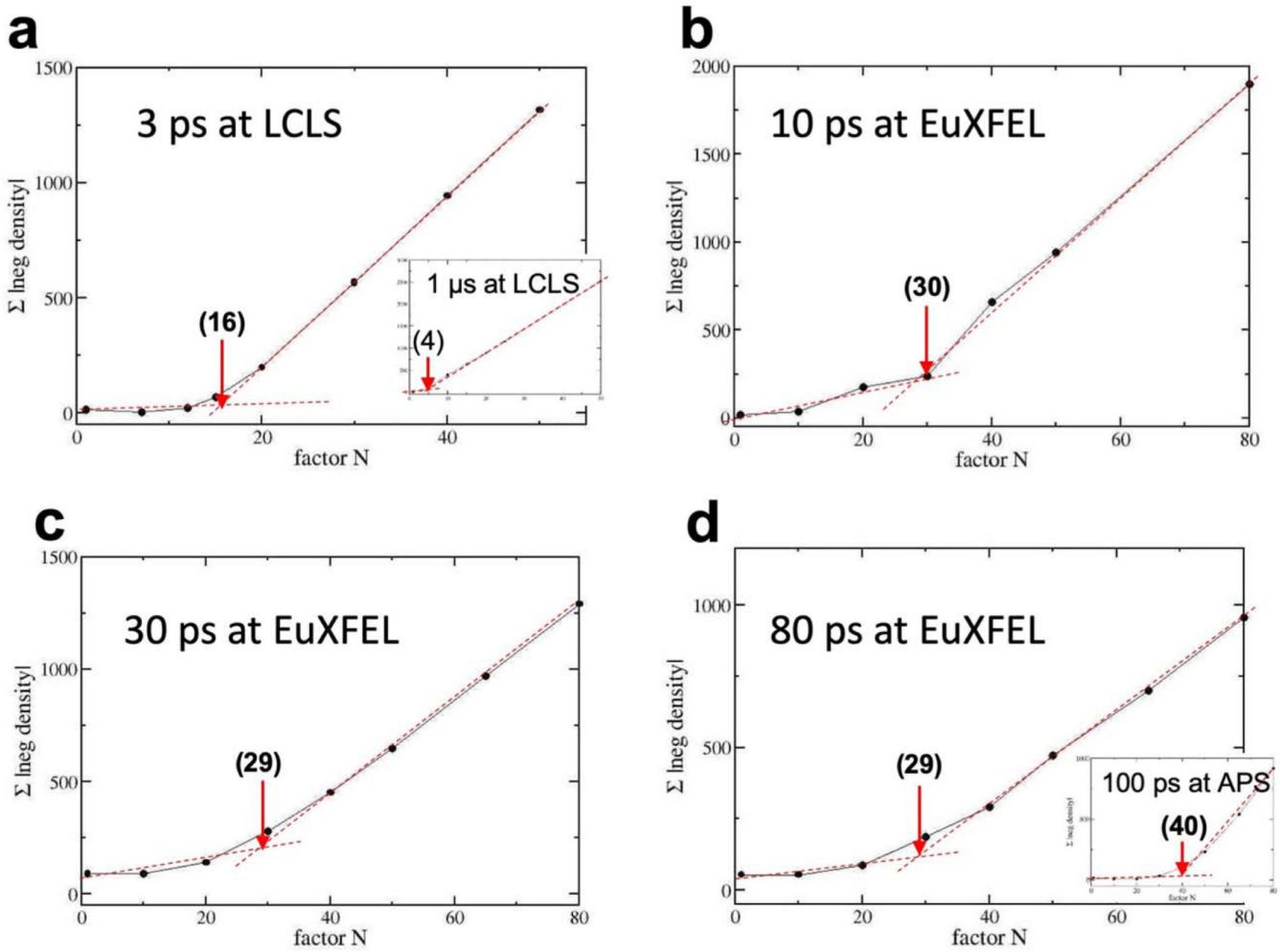

Extended Figure 7. Method to determine the factor N and the population transfer (PT).

The factor N has been determined to calculate extrapolated, conventional maps from data collected at various X-ray sources. Black spheres: summed absolute negative DED in a sphere of R = 4 Å centered on the PCA chromophore double bond. Red dotted lines: the more horizontal line follows the initial slope of the data; the second line delineates the constant incline with larger Ns. The Next (in brackets) can be estimated from the intersection of the two lines. **a**, 3ps data from CXI at LCLS collected with fs laser excitation in the absorption maximum (Pande et al., 2016). Factor N = 16, PT = 12.5 %, insert: 1 μs data collected with ns laser excitation. N = 4, and PT = 50% (Tenboer et al., 2014). **b**, **c**, and **d**, Factors N for the 10 ps, 30 ps, and 80 ps data collected at the EXFEL with fs laser excitation outside the absorption maximum. PT is about 7 % throughout. Insert in **d**, 100 ps data collected at APS (about 6% PT, Jung et al., 2013). 13,214, 13,542, 13,722, 13,142, 13,014 and 12,889 observed difference amplitudes are used to determine extrapolated maps for the 100ps, 1μs, 3ps, 10ps, 30ps and 80ps time delays, respectively.

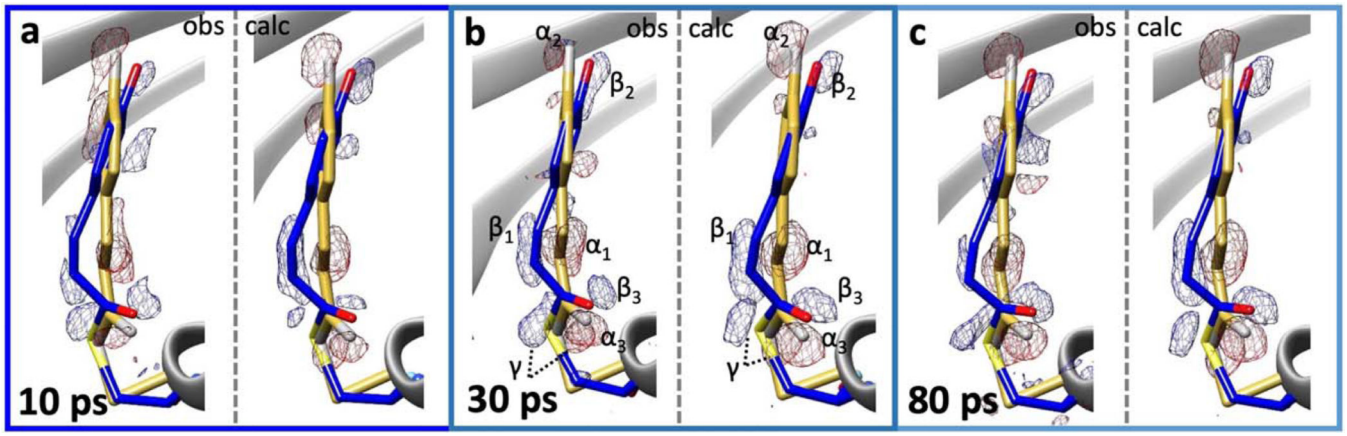

Extended Figure 8. Observed and calculated difference electron densities (DED) near the pCA chromophore.

Left panels: observed difference electron density (blue: 3 σ, red: -3 σ contour levels). Right panels: calculated difference electron density (blue: 4 σ, red: -4 σ contour levels). Yellow model: structure of the dark (reference) state; blue model: structure at a particular time delay. **a**, 10 ps; **b**, 30 ps, c, 80 ps. In panel b pairwise difference density features are marked with α (negative) and β (positive). The feature γ shows the signal caused by the Cys-69 sulfur. The marked DED features can be readily detected at the other time delays. 13,142, 13,014 and 12,889 difference amplitudes were used to calculate the observed DED maps for **a**, **b** and **c**, respectively.

Extended Data Table 1|

Summary of data sets collected[&].

X-ray pulse rate	time point	data sets	flow rate [μl/min]	oil to crystal slurry ratio	net data collection time	time per data set
564 kHz	**10 ps** + 3 interleaved	4	35	0	112 min	28 min

X-ray pulse rate	time point	data sets	flow rate [μl/min]	oil to crystal slurry ratio	net data collection time	time per data set
564 kHz	**30 ps** + 3 interleaved	4	40	30% - 8%	215 min	54 min
564 kHz	**80 ps** + 3 interleaved	4	34	30%	148 min	37 min
1.13 MHz	**Control experiment, 0.89 μs - 2.67 μs**	3	35	0	40 min	13 min
1.13 MHz	pure dark	1	35	0	12 min	12 min

&The ps time-delays are followed by three more X-ray exposures on the μs time-scale. For the 30 ps and 80 ps time-delays, the crystalline slurry was mixed with various amounts of fluorinated mineral oil to experiment with larger flow rates through the capillary tubing, to prevent clogging and to prevent accumulation of debris on the nozzle tip.

Extended Data Table 2|

Statistics of the control data collected with 1.13 MHz X-ray pulses

Control experiments				
Repetition rates X-ray/laser	1.13 MHz/376 kHz			
Temperature	285 K			
Data collection				
Space group	$P6_3$ (173)			
Cell dimensions				
a, *b*, *c* (Å)	66.9, 66.9, 40.8			
α, *β*, *γ* (°)	90, 90, 120			
Resolution (Å)	1.71 (1.71 – 1.74) Å			
	0.89 μs	1.78 μs	2.67 μs	pure dark
Number of hits	13,642	13,734	14,183	5,725
Hit/indexing rate [%]	1.1/60.0	1.1/60.0	1.2/60.0	0.6/85.7
Reflections observed	992,449	1,010,839	973,205	662,072
No of unique reflections	11,502	11,510	11,497	11,504
R_{split} *(%)*	14.9 (76.8)	14.7 (76.8)	14.6 (70.6)	18.1 (111.1)
CC1/2 (%)	97.9 (50.0)	98.0 (51.4)	97.9 (48.6)	96.1 (33.8)
Completeness (%)	99.5 (98.7)	99.6 (98.7)	99.5 (98.4)	99.5 (100.0)
Redundancy	86.3 (13.9)	87.8 (13.2)	84.6 (12.7)	57.6 (19.0)

Extended Data Table 3|

Statistics of data collected with 564 kHz X-ray pulses.

time delays	
Repetition rates X-ray/Laser	564 kHz/141 kHz
Resolution	1.6 (1.6 – 1.63) A
Temperature	285 K
Space group	P63 (173)

time delays				
Unit cell	a = 66.9 Å b = 66.9 Å c = 40.8 Å α=90° β=90° γ=120°			
	10 ps	**dark1 (1.78 μs)**	**dark2 (3.56 μs)**	**dark3 (5.33 μs)**
Hits	93,130	91,184	92,365	88,373
Hit/indexing rate [%]	2.8/43.5	2.8/43.4	2.8/43.4	2.7/43.7
reflections observed	4,016,763	3,929,272	4,017,291	3,883,477
Unique reflections	14,124	14,142	14,141	14,157
Redundancy	284.4 (8.5)	277.8 (7.2)	284.1 (8.2)	274.3 (8.3)
Completeness (%)	99.3 (91.9)	99.4 (93.7)	99.4 (93.3)	99.5 (95.6)
R-split (%)	6.9 (64.0)	7.0 (63.9)	7.0 (60.0)	7.3 (67.1)
CC1/2 (%)	99.6 (60.3)	99.6 (60.0)	99.6 (58.4)	99.5 (58.4)
	30 ps	**dark1 (1.78 μs)**	**dark2 (3.56 μs)**	**dark3 (5.33 μs)**
Hits	81,066	79,580	80,027	77,608
Hit/indexing rate [%]	1.8/50.7	1.8/50.8	1.8/50.9	1.8/51.5
reflections observed	3,948,268	3,892,799	3,921,154	3,853,579
Unique reflections	13,727	13,722	13,726	13,725
Redundancy	287.6 (17.9)	283.7 (17.2)	285.7 (17.7)	280.8 (18.2)
Completeness (%)	98.1 (99.6)	98.1 (99.4)	98.1 (99.4)	98.1 (99.8)
R-split	5.6 (40.2)	5.8 (43.5)	5.8 (38.8)	6.0 (40.9)
CC1/2	99.6 (76.1)	99.6 (75.4)	99.6 (80.6)	99.5 (79.8)
	80 ps	**dark1 (1.78 μs)**	**dark2 (3.56 μs)**	**dark3 (5.33 μs)**
Hits	30,860	29,264	28,332	28,235
Hit/indexing rate [%]	1.1/60.4	1.0/60.1	1.0/62.2	1.0/60.3
reflections observed	2,148,177	2,020,504	2,052,291	1,969,452
Unique reflections	13,711	13,700	13,705	13,703
*Redundancy	156.7 (15.1)	147.5 (14.1)	149.7 (15.1)	143.7 (14.7)
Completeness (%)	98.0 (97.3)	97.9 (97.1)	98.0 (97.3)	97.9 (97.5)
R-split	8.88 (49.9)	9.58 (49.8)	9.62 (49.5)	9.73 (50.3)
CC1/2	99.1 (68.4)	98.9 (70.8)	98.9 (70.5)	98.8 (67.0)

Extended Data Table 4|

Refinement statistics for structures determined at picosecond delays after laser excitation.

	10 ps	**30 ps**	**80 ps**
Refinement			
Resolution (Å)	1.6	1.6	1.6
No. reflections	12,866	12,318	12,072
R_{work} / R_{free}	0.28/0.34	0.22/0.26	0.27/0.32
No. atoms			

	10 ps	30 ps	80 ps
Protein	1,005	1,005	1,005
Ligand/ion	17	17	17
Water	91	91	91
R.m.s. deviations			
Bond lengths (Å)	0.02	0.03	0.02
Bond angles (°)	1.96	2.54	2.25

Extended Data Table 5|

Refinement statistics for structures determined from data without laser excitation.

	Pure Dark (1.13 MHz)	Dark 3 (564 kHz, 5.33 μs)*
Refinement		
Resolution (Ä)	1.7	1.6
No. reflections	10,361	12,625
R_{work} / R_{free}	0.17/0.24	0.16/0.20
No. atoms		
Protein	1005	1005
Ligand/ion	17	17
Water	91	91
R.m.s. deviations		
Bond lengths (Ä)	0.02	0.02
Bond angles (°)	1.86	1.87

* from the 30 ps, darkl, dark2, dark3 time-series

Extended Data Table 6.

Comparison of TRX experiments at various light sources.

Time-delay	Instrument	Laser pulse duration	Laser fluence [mJ/mm^2]	Wavelength [nm]	Population transfer [%]	reference
3 ps	CXI, LCLS	140 fs	0.8	450	12.5	74
10 ps	SPB/SFX, EuXFEL	300 fs	1.6	420	6.7	this study
30 ps	SPB/SFX, EuXFEL	300 fs	1.6	420	7.1	this study
80 ps	SPB/SFX, EuXFEL	300 fs	1.6	420	7.1	this study
100 ps	BioCARS, APS	35 ps	2	390	6.3*	76

* macroscopic crystals investigated by the Laue method CXI[84]: coherent X-ray imaging instrument at the LCLS; SPB/SFX[55]: Single Particles, Clusters, and Biomolecules & Serial Femtosecond Crystallography at the European XFEL; BioCARS[85]: 14-ID-B Laue beamline, sector 14, at the Advanced Photon Source.

Extended Data Table 7|

Protein consumption estimates per successfully collected timedelay compared between EuXFEL and XFELS with 120 Hz repetition rates (with a warm copper LINAC). Net time and protein consumption for 10,000 indexed patterns (per dataset) are compared. In practice 25,000 and more patterns may be required for a high-quality data set. The hit rate and the indexing rate are assumed to be 2% and 50%, respectively. If the hit rate increases, the data collection time and the protein consumption decrease accordingly. Final design specifications at the EuXFEL are assumed. The apparent data collection rate (3520 frames/s) at EuXFEL is determined by the AGIPD that can store 352 diffraction patterns from the X-ray pulses in a train. With an injector flow rate of 30 ^l/min, 1.8 mL are consumed per hour. 1.8 mL of dense protein slurry contain about 100 mg of PYP. The injector flow rate at the warm copper XFEL is one third (10 µL/min) of that of the EuXFEL with an accordingly smaller protein consumption of 33 mg/h.

				EuXFEL		**warm LINAC**	
Experiment	Total	Indexed	Datasets	Net data collection time	PYP	Net data collection time	PYP
pump/probe - dark 1-dark2-dark3 *	4 M	40 K	4	19 min	32 mg	- na -	- na -
pump/probe-dark	2 M	20 K	2	9.5 min	**16 mg**	4.6 h	150 mg
pump into capillary probe with entire train **	1 M	10 K	1	4.7 min	**8 mg**	2.3 h	75 mg

* This data collection scheme has been selected for exploration at the EuXFEL. This does not need to be employed at other (slower) XFELs.

** time delay much longer than the train length (0.6 ms).

Supplementary Material

Refer to Web version on PubMed Central for supplementary material.

Acknowledgement.

We acknowledge European XFEL in Schenefeld, Germany, for provision of X-ray free- electron laser beamtime at Scientific Instrument SPB/SFX and would like to thank the instrument group and facility staff for their assistance. This work was supported by NSF Science and Technology Centers grant NSF-1231306 (“Biology with X-ray Lasers”). CFEL is supported by the Gottfried Wilhelm Leibniz Program of the DFG; the project “X-probe” funded by the European Union’s 2020 Research and Innovation Program under the Marie Sklodowska-Curie grant agreement 637295; the European Research Council, “Frontiers in Attosecond X-ray Science: Imaging and Spectroscopy (AXSIS)”, ERC-2013-SyG 609920 (together with P. Fromme); and the Human Frontiers Science Program grant RGP0010 2017. We acknowledge the support of funding from the Biodesign Center for Applied Structural Discovery at Arizona State University and NSF award #1565180. Funding is also acknowledged from the National Institutes of Health grants R01GM095583 and R01GM117342.

References.

1. Moffat K. Time-resolved biochemical crystallography: A mechanistic perspective. Chemical reviews 101, 1569–1581, doi:Doi 10.1021/Cr990039q (2001). [PubMed: 11709992]
2. Schmidt M. Time-Resolved Macromolecular Crystallography at Modern X-Ray Sources. Methods Mol Biol 1607, 273–294, doi:10.1007/978-1-4939-7000-1_11 (2017). [PubMed: 28573577]

3. Aquila A. et al. Time-resolved protein nanocrystallography using an X-ray free-electron laser. Optics express 20, 2706–2716, doi:10.1364/OE.20.002706 (2012). [PubMed: 22330507]
4. Tenboer J. et al. Time-resolved serial crystallography captures high-resolution intermediates of photoactive yellow protein. Science 346, 1242–1246, doi:10.1126/science.1259357 (2014). [PubMed: 25477465]
5. Chapman HN et al. Femtosecond X-ray protein nanocrystallography. Nature 470, 73–77, doi:10.1038/nature09750 (2011). [PubMed: 21293373]
6. Boutet S. et al. High-resolution protein structure determination by serial femtosecond crystallography. Science 337, 362–364, doi:10.1126/science.1217737 (2012). [PubMed: 22653729]
7. Lomb L. et al. Radiation damage in protein serial femtosecond crystallography using an x-ray free-electron laser. Physical review. B, Condensed matter and materials physics 84, 214111, doi:10.1103/PhysRevB.84.214111 (2011).
8. Nass K. et al. Indications of radiation damage in ferredoxin microcrystals using high-intensity X-FEL beams. J Synchrotron Radiat 22, 225–238, doi:10.1107/S1600577515002349 (2015). [PubMed: 25723924]
9. Suga M. et al. Light-induced structural changes and the site of O=O bond formation in PSII caught by XFEL. Nature 543, 131–135, doi:10.1038/nature21400 (2017). [PubMed: 28219079]
10. Chreifi G. et al. Crystal structure of the pristine peroxidase ferryl center and its relevance to proton-coupled electron transfer. Proceedings of the National Academy of Sciences of the United States of America 113, 1226–1231, doi:10.1073/pnas.1521664113 (2016). [PubMed: 26787871]
11. Wiedorn MO et al. Megahertz serial crystallography. Nat Commun 9, 4025, doi:10.1038/s41467-018-06156-7 (2018). [PubMed: 30279492]
12. Grunbein ML et al. Megahertz data collection from protein microcrystals at an X-ray free-electron laser. Nat Commun 9 (2018).
13. Barends TR et al. Direct observation of ultrafast collective motions in CO myoglobin upon ligand dissociation. Science, doi:10.1126/science.aac5492 (2015).
14. Pande K. et al. Femtosecond Structural Dynamics Drives the Trans/Cis Isomerization in Photoactive Yellow Protein. Science 352, 725–729 (2016). [PubMed: 27151871]
15. Meyer TE, Yakali E, Cusanovich MA & Tollin G. Properties of a water-soluble, yellow protein isolated from a halophilic phototrophic bacterium that has photochemical activity analogous to sensory rhodopsin. Biochemistry 26, 418–423 (1987). [PubMed: 3828315]
16. Genick UK et al. Structure of a protein photocycle intermediate by millisecond time-resolved crystallography. Science 275, 1471–1475 (1997). [PubMed: 9045611]
17. Ihee H. et al. Visualizing reaction pathways in photoactive yellow protein from nanoseconds to seconds. Proceedings of the National Academy of Sciences of the United States of America 102, 7145–7150, doi:10.1073/pnas.0409035102 (2005). [PubMed: 15870207]
18. Kort R. et al. Evidence for trans-cis isomerization of the p-coumaric acid chromophore as the photochemical basis of the photocycle of photoactive yellow protein. Febs Lett 382, 73–78 (1996). [PubMed: 8612767]
19. Polli D. et al. Conical intersection dynamics of the primary photoisomerization event in vision. Nature 467, 440–443, doi:10.1038/nature09346 (2010). [PubMed: 20864998]
20. Mathes T. et al. Femto- to Microsecond Photodynamics of an Unusual Bacteriophytochrome. J. Phys. Chem. Lett. 6, 5, doi:10.1021/jz502408n (2014).
21. Ali AM et al. Optogenetic Inhibitor of the Transcription Factor CREB. Chem Biol 22, 1531–1539, doi:10.1016/j.chembiol.2015.09.018 (2015). [PubMed: 26590638]
22. Schotte F. et al. Watching a signaling protein function in real time via 100-ps time-resolved Laue crystallography. Proceedings of the National Academy of Sciences of the United States of America 109, 19256–19261, doi:10.1073/pnas.1210938109 (2012). [PubMed: 23132943]
23. Creelman M, Kumauchi M, Hoff WD & Mathies RA Chromophore Dynamics in the PYP Photocycle from Femtosecond Stimulated Raman Spectroscopy. Journal of Physical Chemistry B 118, 659–667 (2014). [PubMed: 24451027]
24. Palmer G. et al. Pump-probe laser system at the FXE and SPB/SFX instruments of the European X-ray Free-Electron Laser Facility. J Synchrotron Radiat 26, 328–332 (2019). [PubMed: 30855239]

25. Schmidt M. et al. Protein energy landscapes determined by five-dimensional crystallography. Acta crystallographica. Section D, Biological crystallography 69, 2534–2542, doi:10.1107/S0907444913025997 (2013). [PubMed: 24311594]
26. Prokhorenko VI et al. Coherent control of retinal isomerization in bacteriorhodopsin. Science 313, 1257–1261, doi:10.1126/science.1130747 (2006). [PubMed: 16946063]
27. Mancuso AP et al. The Single Particles, Clusters and Biomolecules and Serial Femtosecond Crystallography instrument of the European XFEL: initial installation. J Synchrotron Radiat 26, 660–676, doi:10.1107/S1600577519003308 (2019). [PubMed: 31074429]
28. Allahgholi A. et al. The Adaptive Gain Integrating Pixel Detector at the European XFEL. J Synchrotron Radiat 26, 74–82, doi:10.1107/S1600577518016077 (2019).
29. Stan CA et al. Liquid explosions induced by X-ray laser pulses. Nat Phys 12, 966–971 (2016).
30. Tripathi S, Srajer V, Purwar N, Henning R. & Schmidt M. pH dependence of the photoactive yellow protein photocycle investigated by time-resolved crystallography. Biophysical journal 102, 325–332, doi:10.1016/j.bpj.2011.11.4021 (2012). [PubMed: 22339869]
31. Schmidt M. Structure based enzyme kinetics by time-resolved X-ray crystallography, in: ultrashort laser pulses in medicine and biology. 201–241 (Berlin; New York: Springer, c2008, 2008).
32. Schmidt M. Time-Resolved Macromolecular Crystallography at Pulsed X-ray Sources. Int J Mol Sci 20, doi:10.3390/ijms20061401 (2019).
33. Jung YO et al. Volume-conserving trans-cis isomerization pathways in photoactive yellow protein visualized by picosecond X-ray crystallography. Nature chemistry 5, 212–220, doi:10.1038/nchem.1565 (2013).
34. Hutchison CDM & van Thor JJ Populations and coherence in femtosecond time resolved X-ray crystallography of the photoactive yellow protein. Int Rev Phys Chem 36, 117–143 (2017).
35. Groenhof G. et al. Photoactivation of the photoactive yellow protein: why photon absorption triggers a trans-to-cis Isomerization of the chromophore in the protein. Journal of the American Chemical Society 126, 4228–4233, doi:10.1021/ja039557f (2004). [PubMed: 15053611]
36. Markovitch O. & Agmon N. Structure and energetics of the hydronium hydration shells. Journal of Physical Chemistry A 111, 2253–2256 (2007). [PubMed: 17388314]
37. Levantino M. et al. Ultrafast myoglobin structural dynamics observed with an X-ray free-electron laser. Nat Commun 6, 6772, doi:10.1038/ncomms7772 (2015). [PubMed: 25832715]
38. DePonte DP et al. Gas dynamic virtual nozzle for generation of microscopic droplet streams. J Phys D Appl Phys 41 (2008).
39. Schmidt M, Rajagopal S, Ren Z. & Moffat K. Application of singular value decomposition to the analysis of time-resolved macromolecular X-ray data. Biophysical journal 84, 2112–2129, doi:10.1016/S0006-3495(03)75018-8 (2003). [PubMed: 12609912]
40. Rajagopal S, Schmidt M, Anderson S, Ihee H. & Moffat K. Analysis of experimental time-resolved crystallographic data by singular value decomposition. Acta crystallographica. Section D, Biological crystallography 60, 860–871, doi:10.1107/S0907444904004160 (2004). [PubMed: 15103131]
41. Kang Y. et al. Crystal structure of rhodopsin bound to arrestin by femtosecond X-ray laser. Nature 523, 561–567, doi:10.1038/nature14656 (2015). [PubMed: 26200343]
42. Kupitz C. et al. Structural enzymology using X-ray free electron lasers. Struct Dyn 4, 044003, doi:10.1063/1.4972069 (2017).
43. Olmos JL Jr. et al. Enzyme intermediates captured “on the fly” by mix-and-inject serial crystallography. BMC Biol 16, 59, doi:10.1186/s12915-018-0524-5 (2018). [PubMed: 29848358]
44. Paul K. et al. Coherent control of an opsin in living brain tissue. Nat Phys 13, 1111–1116, doi:10.1038/NPHYS4257 (2017). [PubMed: 29983725]
45. Wang J. et al. Time-resolved protein activation by proximal decaging in living systems. Nature 569, 509–513, doi:10.1038/s41586-019-1188-1 (2019). [PubMed: 31068699]
46. Tenboer J. et al. Time-resolved serial crystallography captures high-resolution intermediates of photoactive yellow protein. Science 346, 1242–1246, doi:10.1126/science.1259357 (2014). [PubMed: 25477465]

47. Kort R. et al. Evidence for trans-cis isomerization of the p-coumaric acid chromophore as the photochemical basis of the photocycle of photoactive yellow protein. Febs Lett 382, 73–78 (1996). [PubMed: 8612767]
48. Mancuso AP, Aquila A, Borchers G, Giewekemeyer K. & Reimers N. Technical Design Report: Scientific Instrument Single Particles, Clusters, and Biomolecules (SPB). XFEL.EU Technical Report, 232, doi:10.3204/XFEL.EU/TR-2013-004 (2013).
49. Mancuso AP et al. The Single Particles, Clusters and Biomolecules and Serial Femtosecond Crystallography instrument of the European XFEL: initial installation. J Synchrotron Radiat 26, 660–676, doi:10.1107/S1600577519003308 (2019). [PubMed: 31074429]
50. DePonte DP et al. Gas dynamic virtual nozzle for generation of microscopic droplet streams. J Phys D Appl Phys 41 (2008).
51. Echelmeier A. et al. Hydrophobic surface coatings for stable aqueous in oil droplet generation in 3D printed devices. J Appl Crystallogr (in print) (2019).
52. Wiedorn MO et al. Megahertz serial crystallography. Nat Commun 9, 4025, doi:10.1038/s41467-018-06156-7 (2018). [PubMed: 30279492]
53. Hutchison CDM et al. Photocycle populations with femtosecond excitation of crystalline photoactive yellow protein. Chem Phys Lett 654, 63–71, doi:10.1016/j.cplett.2016.04.087 (2016).
54. Schmidt M. et al. Protein energy landscapes determined by five-dimensional crystallography. Acta crystallographica. Section D, Biological crystallography 69, 2534–2542, doi:10.1107/S0907444913025997 (2013). [PubMed: 24311594]
55. Bean RJ, Aquila A, Samoylova L. & Mancuso AP Design of the mirror optical systems for coherent diffractive imaging at the SPB/SFX instrument of the European XFEL. J Optics-Uk 18 (2016).
56. Greiffenberg D. & Collaboration A. The AGIPD detector for the European XFEL. J Instrum 7, Doi 10.1088/1748-0221/7/01/C01103 (2012).
57. Allahgholi A. et al. The Adaptive Gain Integrating Pixel Detector at the European XFEL. J Synchrotron Radiat 26, 74–82, doi:10.1107/S1600577518016077 (2019). [PubMed: 30655470]
58. Heisen BC et al. Data Analysis Support in Karabo at European XFEL. (2013).
59. Boukhelef D, Szuba J, Wrona K. & Youngman C. Software development for high speed data recording and processing. (2013).
60. Kirkwood HJ et al. Initial observations of the femtosecond timing jitter at the European XFEL. Optics letters 44, 1650–1653 (2019). [PubMed: 30933113]
61. Mariani V. et al. OnDA: online data analysis and feedback for serial X-ray imaging. J Appl Crystallogr 49, 1073–1080, doi:10.1107/S1600576716007469 (2016). [PubMed: 27275150]
62. Barty A. et al. Cheetah: software for high-throughput reduction and analysis of serial femtosecond X-ray diffraction data. J Appl Crystallogr 47, 1118–1131, doi:10.1107/S1600576714007626 (2014). [PubMed: 24904246]
63. Yefanov O. et al. Accurate determination of segmented X-ray detector geometry. Optics express 23, 28459–28470 (2015). [PubMed: 26561117]
64. Brehm W. & Diederichs K. Breaking the indexing ambiguity in serial crystallography. Acta crystallographica. Section D, Biological crystallography 70, 101–109, doi:10.1107/S1399004713025431 (2014). [PubMed: 24419383]
65. Palmer G. et al. Pump-probe laser system at the FXE and SPB/SFX instruments of the European X-ray Free-Electron Laser Facility. J Synchrotron Radiat 26, 328–332 (2019). [PubMed: 30855239]
66. Glownia JM et al. Time-resolved pump-probe experiments at the LCLS. Optics express 18, 17620–17630, doi:10.1364/OE.18.017620 (2010). [PubMed: 20721148]
67. Harmand M. et al. Achieving few-femtosecond time-sorting at hard X-ray free-electron lasers. Nat Photonics 7, 215–218, doi:10.1038/Nphoton.2013.11 (2013).
68. Bionta MR et al. Spectral encoding of x-ray/optical relative delay. Optics express 19, 21855–21865, doi:10.1364/OE.19.021855 (2011). [PubMed: 22109037]

69. Murshudov GN et al. REFMAC5 for the refinement of macromolecular crystal structures. Acta crystallographica. Section D, Biological crystallography 67, 355–367, doi:10.1107/S0907444911001314 (2011). [PubMed: 21460454]
70. Winn MD et al. Overview of the CCP4 suite and current developments. Acta Crystallogr D 67, 235–242, doi:10.1107/S0907444910045749 (2011). [PubMed: 21460441]
71. Ren Z. et al. A molecular movie at 1.8 A resolution displays the photocycle of photoactive yellow protein, a eubacterial blue-light receptor, from nanoseconds to seconds. Biochemistry 40, 13788–13801 (2001). [PubMed: 11705368]
72. Drenth J. (Springer, 1999).
73. Genick UK et al. Structure of a protein photocycle intermediate by millisecond time-resolved crystallography. Science 275, 1471–1475 (1997). [PubMed: 9045611]
74. Pande K. et al. Femtosecond Structural Dynamics Drives the Trans/Cis Isomerization in Photoactive Yellow Protein. Science 352, 725–729 (2016). [PubMed: 27151871]
75. Terwilliger TC & Berendzen J. Bayesian difference refinement. Acta Crystallogr D 52, 1004–1011 (1996). [PubMed: 15299610]
76. Jung YO et al. Volume-conserving trans-cis isomerization pathways in photoactive yellow protein visualized by picosecond X-ray crystallography. Nature chemistry 5, 212–220, doi:10.1038/nchem.1565 (2013).
77. Hutchison CDM & van Thor JJ Populations and coherence in femtosecond time resolved X-ray crystallography of the photoactive yellow protein. Int Rev Phys Chem 36, 117–143 (2017).
78. Emsley P, Lohkamp B, Scott WG & Cowtan K. Features and development of Coot. Acta crystallographica. Section D, Biological crystallography 66, 486–501, doi:10.1107/S0907444910007493 (2010). [PubMed: 20383002]
79. Nogly P. et al. Retinal isomerization in bacteriorhodopsin captured by a femtosecond x-ray laser. Science 361, 145-+, doi:10.1126/science.aat0094 (2018).
80. Schmidt M. Structure based enzyme kinetics by time-resolved X-ray crystallography, in: ultrashort laser pulses in medicine and biology. 201–241 (Berlin; New York: Springer, c2008, 2008).
81. Schmidt M. Time-Resolved Macromolecular Crystallography at Pulsed X-ray Sources. International Journal of Molecular Sciences 20, doi:10.3390/ijms20061401 (2019).
82. Richards FM & Kundrot CE Identification of Structural Motifs from Protein Coordinate Data - Secondary Structure and 1st-Level Supersecondary Structure. Proteins-Structure Function and Genetics 3, 71–84 (1988).
83. Maia FR The Coherent X-ray Imaging Data Bank. Nature methods 9, 854–855, doi:10.1038/nmeth.2110 (2012). [PubMed: 22936162]
84. Liang M. et al. The Coherent X-ray Imaging instrument at the Linac Coherent Light Source. J Synchrotron Radiat 22, 514–519, doi:10.1107/S160057751500449X (2015). [PubMed: 25931062]
85. Graber T. et al. BioCARS: a synchrotron resource for time-resolved X-ray science. J Synchrotron Radiat 18, 658–670, doi:10.1107/S0909049511009423 (2011). [PubMed: 21685684]

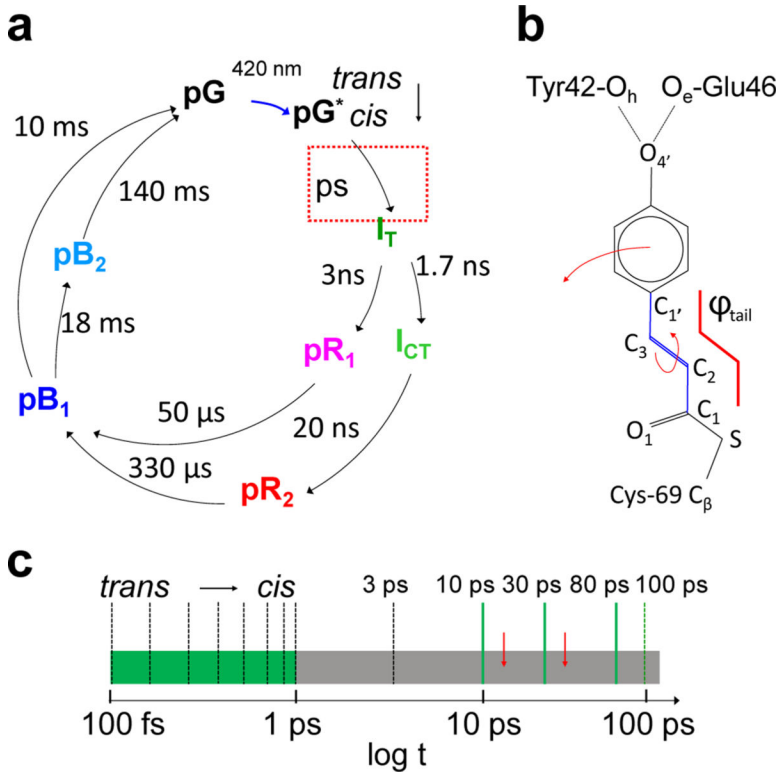

Fig. 1|. The photocycle of PYP in crystals.

a, The photocycle (simplified) is initiated by blue light that excites the ground (dark) state pG to the electronic excited state pG*. After the *trans* to *cis* isomerization at 600 fs, several electronic ground state intermediate states called I_T, pR_1, pR_2, pB_1 and pB_2 are populated on various time scales until the photocycle completes. Approximate relaxation times are shown. Red dotted box: relaxations on the picosecond time scale. **b,** The chemical structure of the pCA chromophore bound to the Cys-69 sulfur. The *trans* configuration is shown. The torsional angle φ_{tail} as defined by chromophore carbon atoms C_1-C_2=C_3-C_1' is outlined in red. Hydrogen bonds between the pCA head and Glu46 and Tyr42 are marked. The rotation about the double bond as well as the head displacement at longer times are shown by arrows. **c,** The ultrafast time scale from 100 fs to 100 ps. Black dashed bars: time-delays collected at the LCLS (Pande et al., 2016), green dashed bar: time-delay collected at APS (Jung et al., 2013). Green solid bars: time-delays as collected in this study. They cover the poorly explored time-range from 1 ps to 100 ps (gray). Red arrows: picosecond processes observed spectroscopically (Creelman et al., 2014).

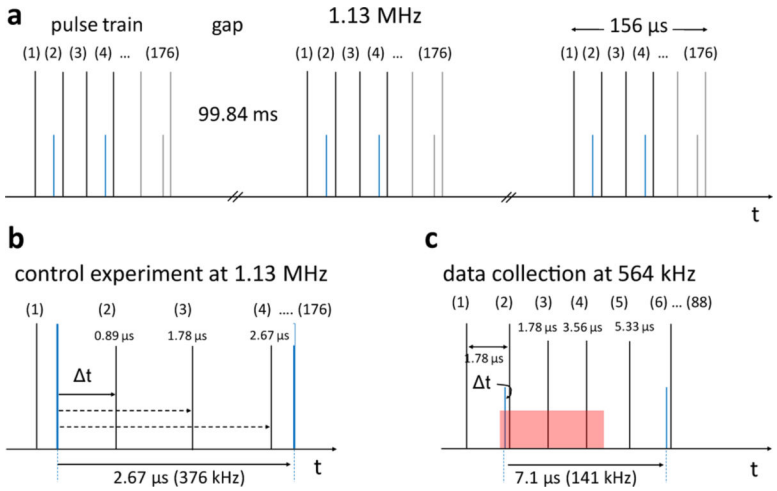

Fig. 2|. Pulse train structure and laser excitation.

a, X-ray pulse trains (black vertical lines) at EuXFEL with 1.13 MHz pulse repetition rate. A pulse train is 156 µs long, contains 176 X-ray pulses and repeats 10 times per second. There are 99.84 ms gaps between the pulse trains. Blue: laser pulses for a pump-probe dark TR-SFX data collection scheme. Note: when EuXFEL design specifications are reached, 2700 pulses with up to 4.5 MHz pulse repetition rate are in a train. At 4.5 MHz, each pulse train is 600 µs long with 99.4 ms gaps between the trains. In total there are 27,000 pulses/s, a subset of which (about 3520/s) can be stored in, and read out, by in the AGIPD detector. **b,** 1.13 MHz control experiment with 376 kHz laser excitation. After the laser pulse, subsequent X-ray pulses arrive at 887 ns, at 1.78 µs and at 2.67 µs. The sequence repeats until the end of the pulse train. **c,** 564 kHz data collection with three interleaved X-ray pulses. 88 pulses are in the train, only. The laser pulses are separated by 7.1 µs (141 kHz) to provide enough time for the laser excited volume (red) to move out of the X-ray interaction region. 519,336 diffraction patterns were averaged to determine the scheme.

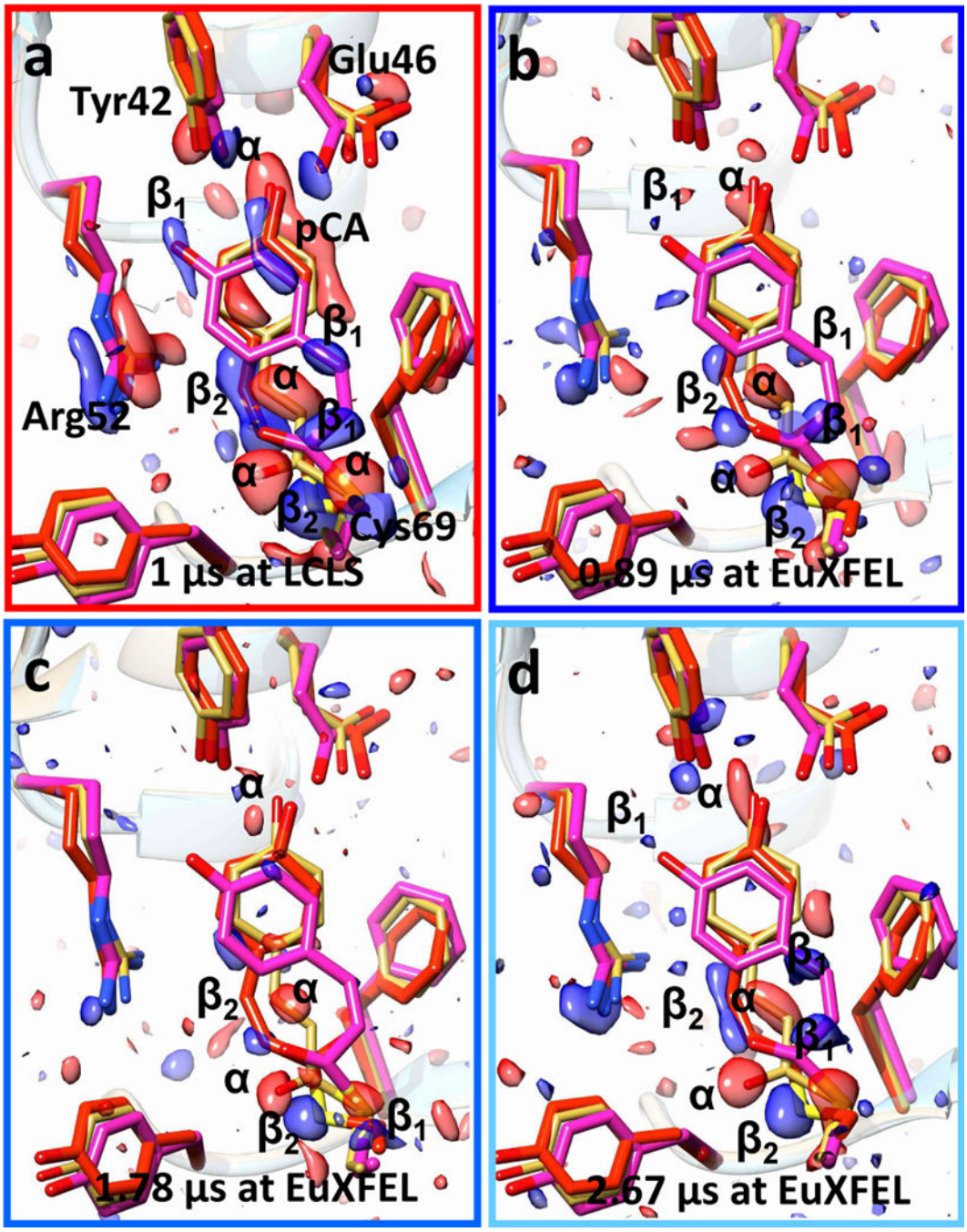

Fig. 3|. TR-SFX experiments at LCLS and EuXFEL.

a, Difference electron density (DED) in the PYP chromophore pocket at 1 μs time-delay as determined at the LCLS (Tenboer et al., 2014). Red: negative DED, blue: positive DED on the −3σ/3σ contour levels, respectively. Prominent features are labeled α (negative) or β_1 and β_2 (positive). Features α are on top of the reference structure (yellow), β_1 and β_2 features correspond to intermediate structures called pR1 (magenta) and pR2 (red), respectively. The pattern of α and β_1, β_2 features persists in all maps at all times. **b – d**, Results of the control experiment with 1.13 MHz X-ray pulse repetition and 376 kHz laser

excitation (see also Fig. S2b). **b,** 0.89 μs after the laser pulse, **c,** 1.78 μs after the laser pulse, **d,** 2.67 μs after the laser pulse.

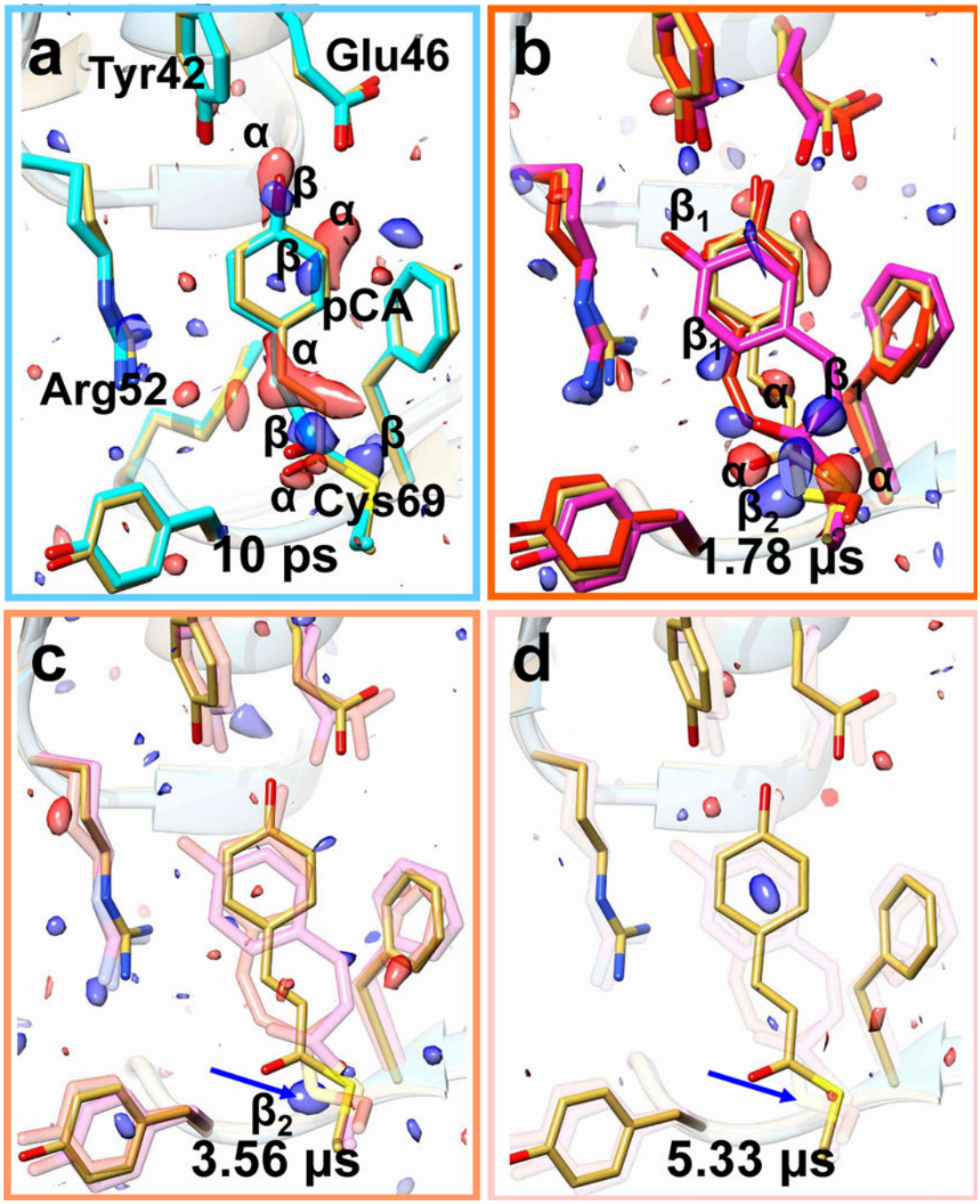

Fig. 4|. Difference electron density (DED) and structures of the chromophore binding region of PYP.

TR-SFX data were collected with 564 kHz X-ray and 141 kHz laser pulse repetition rates, respectively. **a,** 10 ps time delay. Yellow: reference structure, green: 10 ps structure. Red features α: negative difference DED (- 3σ contour level), blue, β: positive DED (3 σ contour level). **b,** The pattern of DED features radically changes compared to (a). Magenta and red: structures of the pR1 (DED features β_1) and pR2 (DED features β_2) intermediates,

respectively. **c,** After 3.56 μs only the prominent feature of the Cys69 sulfur remains, which is completely absent at 5.33 μs, see blue arrows in **c** and **d**.

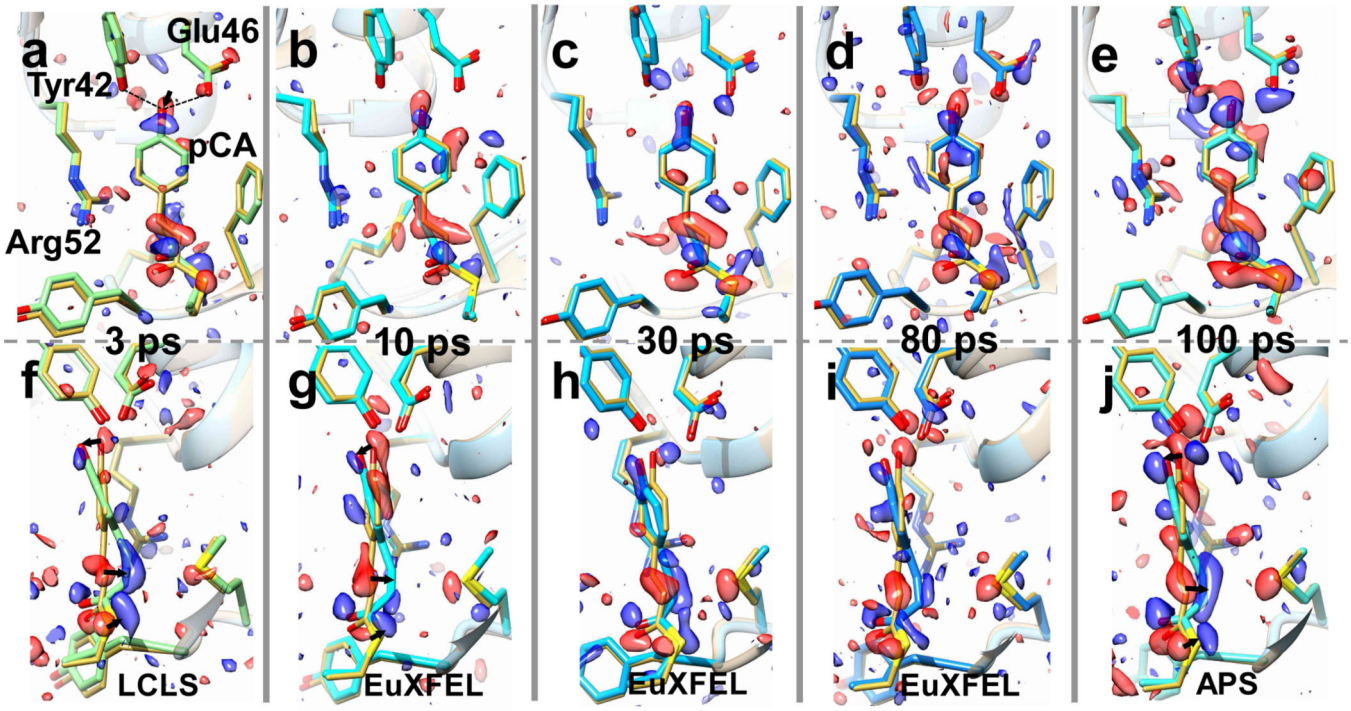

Fig. 5|. Time series of TRX data from 3 ps to 100 ps collected at LCLS, EuXFEL and APS. Structures and difference electron density (DED) in the chromophore binding region of PYP. Red: negative DED (−3σ contour level), blue positive DED (3 σ contour level). Important residues and the pCA chromophore are marked in **a**. Yellow structure: structure of the (dark) reference state. Arrows depict structural displacements in **a**, **f** and **j**. Upper: front view, lower side view. **a** and **f**, 3 ps delay as collected at LCLS. Green: PYP structure at 3 ps (Pande et al., 2016). **b** and **g**, 10 ps time delay, this study, cyan: PYP structure at 10 ps. **c** and **h**, 30 ps time delay, this study, sky blue: PYP structure at 30 ps. **d** and **i**, 80 ps time delay, this study, blue: PYP structure at 80 ps. **e** and **j**, 100 ps time-delay as determined at APS, light blue: PYP structure at 100 ps (Jung et al., 2012).

Table 1.

Geometry of the pCA chromophore after refinement.

	dark	3 ps	10 ps	30 ps	80 ps	100 ps
$^{a}N_{ext}$	--	16	30	29	29	40
H-bond [Å] pCA to E46	2.55	3.30	2.82	2.87	2.86	2.79
H-bond [Å] pCA to Y42	2.58	2.57	2.65	2.62	2.64	2.39
φ_{tail} [°]	172	39	51	54	40	30

[a] characteristic N used to calculate extrapolated maps

The length of the hydrogen bonds from the pCA head hydroxyl to Glu 46 and Tyr 46 as well as the torsional angle φ of the pCA tail defined by pCA carbon atoms C1, C2, C3 and C1' is shown. For the tail in the *trans* configuration φ is close to 180°, in the *cis* configuration φ it is close to 0°.